



# Framework for reliable and automatic multi-frequency correction of non-anechoic antenna measurements

Adrian Bekasiewicz<sup>a,\*</sup>, Mariusz Dzwonkowski<sup>a,b</sup>, Vorya Waladi<sup>a</sup>

<sup>a</sup> Faculty of Electronics, Telecommunications and Informatics, Gdansk University of Technology, Narutowicza 11/12 80-233 Gdansk, Poland

<sup>b</sup> Department of Radiology Informatics and Statistics, Faculty of Health Sciences, Medical University of Gdansk, Gdansk, Poland

## ARTICLE INFO

### Keywords:

Non-anechoic measurements  
Post-processing  
Automatic-calibration  
Bandwidth tuning  
Antenna measurements  
Compact antennas  
Internet of Things

## ABSTRACT

Correction of antenna far-field measurements performed in uncontrolled environments is a challenging problem. Non-anechoic sites, while cheap compared to professional laboratories, suffer from poor propagation properties due to multipath interferences and noise from external sources of electromagnetic radiation. Direct measurements in such conditions are ineffective for drawing meaningful conclusions on antenna performance. The quality of obtained responses can be significantly enhanced through application of appropriate post-processing approaches. Unfortunately, performance of available techniques is subject to experience-based adjustment of algorithm-specific setup, often aided with rule-of-thumb solutions determined based on rudimentary experiments. In this work, limitations of existing manual, or semi-manual approaches to post-processing setup are showcased in contrast with an unsupervised tuning that employs rigorous numerical optimization. The proposed framework automates the determination of correction settings based on analysis of discrepancy between the refined antenna measurements against the responses obtained from electromagnetic simulations. It is the first deterministic, numerically-driven tool tailored for post-processing of data obtained in non-anechoic environments while eliminating the need for cognitive experimentation. A thorough evaluation of the method was performed in two test sites, incorporating five different setups and five correction techniques, for a total of 1250 experiments executed across 25 independent frequencies of interest and three antenna structures. Benchmark results that demonstrate usefulness of automatic setup adjustment when compared to rule-of-thumb methods are also provided.

## 1. Introduction

Measurements represent one of the key steps in the development of antennas. Their primary objective is accuracy validation of the electromagnetic (EM) simulation models used in the course of structure development. The comprehensive assessment of performance figures is aimed at examining the real-world behavior of antenna prototypes. The responses of interest typically encompass electrical characteristics such as reflection, and/or isolation between radiators, as well as field-related attributes like radiation pattern, or axial ratio [1,2]. The electrical behavior can be explicitly validated using, e.g., vector network analyzers (VNA), whereas extraction of the field-related responses is typically based on a series of measurements carried out in a dedicated laboratories where strict control over propagation conditions is maintained.

The assessment of microwave antenna radiation performance

typically involves either near-field [3–5], or far-field [6–8] analysis. Methods that belong to the second category are arguably more straightforward to implement, require less intricate setups, and provide a good representation of real-world conditions. A typical representation of far-field antenna measurement system is a two-port network that consists of the antenna under test (AUT) and a reference antenna (RA) separated by the wireless propagation medium. The radiators are installed on dedicated positioning towers that maintain their appropriate angular alignment [8]. The setup also includes active equipment, interconnection cables, and appropriate software for data acquisition and visualization [8,9].

Fidelity of RA-AUT transmission measurements carried out through a wireless medium is subject to deterioration resulting from dynamic propagation conditions [8–11]. The latter ones include environmental factors (e.g., temperature variations, humidity, free-floating contaminants, etc.), as well as multi-path interferences, EM noise from external

\* Corresponding author.

E-mail address: [adrian.bekasiewicz@pg.edu.pl](mailto:adrian.bekasiewicz@pg.edu.pl) (A. Bekasiewicz).

radiation sources, or thermal noise [12]. To mitigate these issues, RA-AUT system is normally installed in expensive, professional facilities that maintain strict control over the propagation environment [8]. Examples include anechoic chambers (AC), compact antenna test ranges (CATR), complex antenna lattices with plane-wave generators, and others [8,13–17].

Although professional facilities are considered crucial for certification-grade antenna tests, high cost of their construction and maintenance seems to be unjustified if the main goal of measurements is to support less demanding applications such as teaching, or budget-constrained research. For the mentioned scenarios, practical understanding of validation-related practices or rough verification of prototype designs take precedence over high accuracy. Furthermore, expensive infrastructure is often discouraged for unskilled personnel, making laboratory-grade facilities primarily intended for professionals.

The cost of far-field experiments can be substantially reduced by neglecting control of the propagation conditions in favor of measurements in non-anechoic regime [9,10,12,18]. Examples include in-door locations such as office rooms, hallways or passages, but also out-door environments that include yards, roofs, parks, etc. Due to lack of mechanisms for suppressing interferences and EM noise, direct measurements performed in uncontrolled conditions are of little-to-no use for drawing conclusions about the far-field AUT performance [10,19,20]. However, useful part of the RA-AUT transmission, also referred to as Line-of-Sight (LoS) signal, can be extracted from noisy responses using suitable post-processing algorithms. The latter facilitate the use of non-anechoic tests as a cost-efficient alternative to professional measurements.

Significant research efforts have been directed towards enhancing the accuracy of antenna measurements in non-anechoic environments [10,18,21–28]. Popular group of correction approaches involve multi-frequency experiments that comprise two key steps: (i) measurement of the RA-AUT transmission over a specified bandwidth around the frequency of interest and (ii) post-processing of the responses—either in the frequency or time domain—to separate the direct transmission from interferences. Existing frequency-based techniques refine the fidelity of antenna far-field characteristics through extraction of causal far-field responses represented using Chebyshev polynomials [23], matrix-pencil decomposition, or Gabor schemes [9,22,26]. Another group of methods involve post-processing of time-domain impulse responses derived from frequency measurements using appropriate kernels [9,11,28]. The latter ones are adjusted to augment the LoS fraction of the response while attenuating its unwanted components. Upon correction, the refined time-domain data are transformed back into the frequency domain, enabling the extraction of radiation patterns.

The outlined correction methods are primarily demonstrated using high-gain antennas [9]–[12,21–23,25], idealized conditions that include anechoic chambers (or semi-ACs) with installed reflective surfaces [9,15,22,23,29–31], or EM simulations [32–35]. For the former, achieving accurate performance reconstruction is considered less of a challenge when compared to uncontrolled environments [20]. Another problem is that the fidelity of refined responses is not only tied to propagation conditions within the test setup at hand, but also precise tuning of algorithm parameters [9,10,18,20,32]. For multi-frequency approaches, the bandwidth, sweep around the frequency of interest, and kernel/basis functions settings are considered of high importance [9,18]. The existing literature mainly addresses the tuning issue through heuristic solutions such as rules-of-thumb, also aided by visual inspection of pre-processed responses rather than more formal numerical procedures [9,10,23,36]. This reliance on cognitive techniques makes determination of appropriate post-processing setup a challenging and time-consuming process. Consequently, manual or semi-manual methods are not only prone to failure, but also unsuitable when enhancement of non-anechoic measurements is considered for *en-masse* experiments [9,20,37].

Recent advancements in multi-frequency measurements include

methods that aim to automatically calibrate post-processing algorithms based on the propagation conditions [20,38,39]. The algorithms primarily involve a detailed analysis of the impulse responses or power spectra in the time domain to differentiate and retain the signal portion corresponding to LoS transmission while minimizing the impact of the unwanted components. The mentioned approaches are oriented towards adapting the kernel function intervals through comparative analyses of antennas with established responses, evaluation of impulse response properties, or using filtering kernels with adaptively tuned parameters [12,20,38,39]. The approaches proved useful for obtaining high-quality measurements while shifting the burden related to adjustment of post-processing algorithms from the engineering-insight (predominantly involving cognitive, manual tuning) to numerical methods. Furthermore, the methods have been successfully validated in uncontrolled environments, also using small antenna structures that poses additional challenge for correction due to low-gain and hence low signal-to-noise ratio of conducted measurements. Despite the demonstrated usefulness, the mentioned methods still share a limitation inherited from older approaches, i.e. the reliance on rules-of-thumb for determining the bandwidth and resolution of the frequency sweep around the frequency of interest. At the same time, more recent findings suggest that appropriate tuning of post-processing setup according to frequency of interest might notably affect the fidelity of corrected responses [39].

In this work, we reassess the rule-of-thumb-based approaches for determination of bandwidth and frequency resolution of non-anechoic antenna measurements through quantitative analyses. We provide a detailed discussion of shortcomings associated to experience-based correction setup which represents the motivation behind development of a framework for unsupervised tuning of the relevant parameters. The proposed method offers fully automatic selection of the bandwidth (and suitable resolution) using rigorous numerical optimization oriented towards fitting the refined non-anechoic measurements to appropriately scaled EM simulation responses. The approach has been thoroughly evaluated in two test-sites using three antenna examples and a total of five multi-point methods that involve both time- and frequency-domain correction. Overall, a total of 1250 experiments have been performed at 25 independent frequencies. The obtained results quantitatively demonstrate the impact of unbiased performance tuning on the quality of correction for both modern [12,39], and well-established post-processing mechanisms [9,44]. Additionally, it is showcased that the optimal bandwidth around frequency of interest may not only be affected by the selected antenna type, but also its frequency of operation and the propagation conditions in the test site at hand. To the best of our knowledge, the proposed framework is the first approach that neglects reliance on cognitive (i.e., manual and/or rule-of-thumb-based) measurements in favor of adjusting the correction parameters in a fully deterministic manner using rigorous numerical techniques. The approach not only contrasts with well-accepted procedures for responses correction tuning, but also represents a notable advancement in terms of improving their performance, especially for measurements conducted in uncontrolled environments [20,38,39,44]. Main contributions of the work include:

- Demonstration, based on experiments, that the appropriate setup of correction algorithms is subject to the selected AUT, operational conditions, as well as frequency of interest;
- Development of a framework for automatic optimization of post-processing setup based on relaxed comparisons against uniformly scaled EM simulation models;
- Extensive validation of the framework in terms of applicability to algorithm-independent operation and usefulness for unsupervised improvement of correction performance;
- Empirical demonstration that optimized post-processing settings are not interchangeable between the test sites.

The structure of the paper is as follows. Section 2 consists

formulation of the problem, a thorough discussion of challenges associated with the cognition-driven post-processing setups, and description of the proposed framework for automatic adjustment of correction settings. Section 3 provides a brief discussion of multi-frequency post-processing algorithms used for comparative analyses. Experimental results are presented in Section 4. Section 5 provides a thorough discussion of the results generated using the proposed method with emphasis on comparisons against the conventional setups and cross-test-site evaluations. Evaluation of method robustness through analysis of variance, as well as discussion concerning potential limitations of the method are also considered. Finally, Section 6 concludes the work and outlines potential directions for future research.

## 2. Methodology

An algorithm for automatic adjustment of correction setup for far-field measurements performed in non-anechoic conditions is presented. The section contains formulation of the design problem, discussion of the challenges associated to post-processing with rule-of-thumb-based setups, as well as explanation of the proposed tuning method. To make the paper self-contained, a brief summary of the post-processing algorithms used in this study is contained in Section 3.

### 2.1. Formulation of the problem

Let  $\mathbf{R}_u(\omega, \theta, \varphi, \rho)$  be a matrix of complex, uncorrected transmission responses obtained between the RA-AUT system components in uncontrolled environment. The parameter vectors  $\omega = [\omega_1 \dots \omega_K]^T$  ( $k = 1, \dots, K$ ),  $\theta = [\theta_1 \dots \theta_A]^T$  ( $a = 1, \dots, A$ ),  $\varphi$ , and  $\rho$  denote sweep around the frequency of operation  $f_0 = (\omega_K - \omega_1)/2$ , elevation- and azimuth-related coordinates of AUT w.r.t. RA, and polarization-oriented rotation of RA. A conceptual illustration of the rotation planes for the available measurement system is shown in Fig. 1 [20,38]. In this study, data acquisition is performed only in a single plane ( $\varphi = 0$  or  $\varphi = \pi/2$ ; depends on the AUT type) for co-polar operation ( $\rho = \pi/2$ ), which simplifies the notation. Hence,  $\mathbf{R}_u = \mathbf{R}_u(\omega, \theta) = \mathbf{R}_u(\omega, \theta, \varphi, \rho = \pi/2)$  can be defined as a  $K \times A$  matrix of the form:

$$\mathbf{R}_u(\omega, \theta) = \begin{bmatrix} R_u(\omega_1, \theta_1) & \dots & R_u(\omega_1, \theta_A) \\ \vdots & \ddots & \vdots \\ R_u(\omega_K, \theta_1) & \dots & R_u(\omega_K, \theta_A) \end{bmatrix} \quad (1)$$

It is worth noting that the frequency step and bandwidth around  $f_0$  are given as  $\delta\omega = \omega_k - \omega_{k-1}$  and  $B = \omega_K - \omega_1$ , respectively. The correction process is oriented towards determination of  $\mathbf{R}_c = \mathbf{R}_c(f_0, \theta)$  response which approximates the anechoic chamber measurements based on appropriate post-processing of responses obtained in the uncontrolled environment. For frequency-based algorithms the  $\mathbf{R}_u \rightarrow \mathbf{R}_c$

transformation can be obtained using the following generic framework:

1. Measure  $\mathbf{R}_u(\omega, \theta)$  in uncontrolled environment, set  $a = 1$ ;
2. Obtain  $\mathbf{R}_c(\omega, \theta_a)$  from  $\mathbf{R}_u(\omega, \theta_a)$  using the selected correction method (cf. Section 3);
3. If  $a < A$ , set  $a = a + 1$  and go to Step 2; otherwise extract  $\mathbf{R}_c(f_0, \theta)$  from  $\mathbf{R}_c(\omega, \theta)$  and END.

For one-shot experiments—i.e., measurements performed in uncontrolled environment only once per each RA-AUT rotation angle—the correction in Step 2 can be performed in time-, or frequency-domain. The far-field responses fidelity is subject to appropriate configuration of the selected post-processing routine. This setup is typically determined in cognitive manner based on rule-of-thumb approaches.

### 2.2. Challenges related to post-processing with cognitive setups

Post-processing performance is subject to determination of suitable algorithm-specific hyperparameters (also referred to as setup, parameters, or settings). For multi-frequency routines the most important ones are bandwidth  $B$  around  $f_0$  and step  $\delta\omega$ . The latter one is associated with the overall number of frequency samples  $K$  used for correction (cf. Section 2.1). In the literature, the bandwidth is often bound from below based on analysis of the delay between LoS signal and its shortest identified (or expected) interference [9,10,18,22,26]. In [9], the lower limit is estimated as  $B_{\min} = (d_2 - d_1)/\nu$ , where  $d_1$  and  $d_2$  represent physical measurement of the RA-AUT distance and the shortest expected path of reflected signal;  $\nu$  denotes the speed of light in vacuum [20]. Another popular method involves determination of bandwidth based on visual inspection of the RA-AUT responses in time domain [9,10]. The method boils down to calculation of  $B_{\min} = 1/(t_2 - t_1)$ , where  $t_1$  and  $t_2$  represent peaks associated with LoS and non-LoS (i.e., multi-path interferences, and/or noise) transmission. Alternatively,  $B_{\min} = \nu/(\beta A)$  is suggested in [20], where  $\beta = 3$  is the scaling coefficient determined based on a set of experiments and  $A$  represents the size of AUT at hand. The argument behind maintaining broader bandwidth for small, low-gain antennas is their lower signal-to-noise ratio which might require narrower time sweep  $\delta t = 1/B$  to capture the “dynamics” of the environment and its effects on corrected measurements fidelity [20].

Estimation of the frequency step (or the number of samples  $K$  over  $B$ ) is limited to rudimentary rules-of-thumb. Arguably, the main reason is their limited effect on correction performance when compared to bandwidth. The recommended steps  $\delta\omega$  vary from sub-MHz up to a few MHz [9,10,22]. The main argument behind determination of specific sweep is that the number of points must be large enough to capture the contribution of signal and interferences on the RA-AUT response while mitigating the effects of aliasing (the latter is deemed important for time-domain-based methods). In [20],  $K$  of around 200 is suggested as suitable to capture environmental dynamics (assuming that relatively short separation between the measurement towers is maintained).

Cognition driven selection of discussed parameters is subject to challenges that include: (i) difficulties in identification of LoS and non-LoS signals, (ii) lack of clear guidelines concerning choice of bandwidth, as well as (iii) variability of setups with test environments and (iv) frequencies of interest. The guidelines concerning determination of bandwidth based on physical measurements within the test site are not only prone to failure but also assume that properties of the propagation environment are well understood by the engineer involved in the experiments (clearly, that does not have to be the case) [20]. Evaluation of the bandwidth based on visual inspection of time-domain response also requires experience. Also, it is hindered for phase-less signals due to difficulties in unequivocal discrimination of delays between LoS and reflected signals [20]. As it comes to determination of appropriate bandwidth for correction, there seem to be no apparent consistency between recommendations from the literature [10,20,22]. For instance, adjustment of  $B$  to the correction method of choice varies from  $B_{\min}$  to

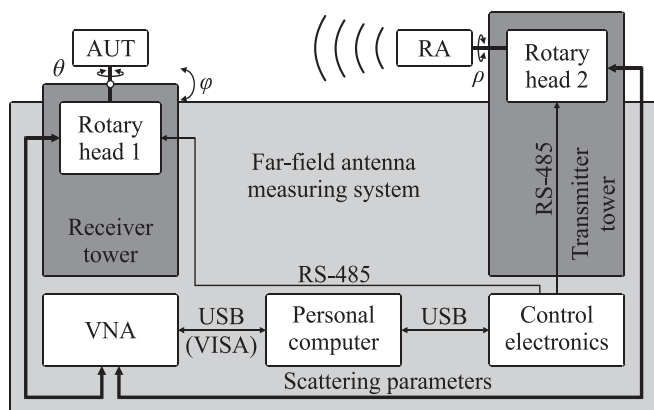


Fig. 1. Block diagram of the measurement setup with emphasis on rotation planes.

$10B_{\min}$  in [9]. At the same time,  $\sim 3B_{\min}$  is selected in [10] with no clear justification. Also, there seem to be no evident (or unequivocally proved) connection between adjustment of bandwidth according to AUT aperture and peak-to-peak delays [20].

Most of the literature-based recommendations are derived based on experiments in idealized conditions that include measurements of antennas in ACs with introduced reflective sheets, or reverberation enclosures [9,10,21,22,23,25,28]. Consequently, adaptation of these setups to uncontrolled environments might pose additional challenges. Recent findings indicate that optimum setup varies with  $f_0$  which might necessitate its re-set for each experiment [39]. The latter is difficult given no feedback on the fidelity of post-processed antenna responses (the main assumption is that AC measurements of the AUT are not present as their availability would contradict the entire concept of post-processing). Consequently, parameters considered suitable for correction at one frequency might be sub-optimal at another. Furthermore, recommendations concerning selection of frequency points for post-processing seem to be inconsistent. As already mentioned, specific step-size values are selected to mitigate the effects of aliasing while capturing the relevant changes of the response (predominantly in time-domain) [9,10,26]. At the same time, the findings of [20] suggest that aliasing is of lesser concern when measurements are performed in uncontrolled conditions due to being encompassed by noise resulting from the dynamics of propagation environment. The above discussion indicates that the main bottleneck in cognition-driven determination of post-processing setup involves determination of parametric recommendations based on specific case studies rather than rigorous evaluations. From this perspective, rules-of-thumb from the literature are not generic, but rather tailored to specific testing environments and/or antennas.

The challenges concerning selection of suitable setup for post-processing of non-anechoic measurements are illustrated in Fig. 2, where changes of identified LoS-to-non-LoS delays as a function of frequency and the selected AUT are demonstrated. Fig. 3 shows variations of the corrected responses fidelity for time-domain post-processing (cf. Section 3.1) as functions of  $f_0$  and  $B$ , as well as  $B$  and  $K$ , respectively, indicating multi-modal and non-differentiable character of landscapes. Difficulties associated with selection of correction setups, as well as inconsistency between tuning methods imply that reliability of measurements post-processing is a subject to substantial engineering experience. From this perspective, a reliable correction of antenna responses obtained in non-anechoic environments remains an open problem.

### 2.3. Automatic adjustment of measurement setup

Automatic adjustment of measurement setup involves numerical

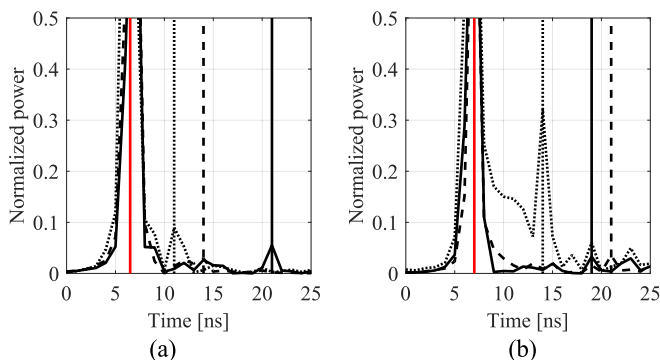


Fig. 2. Manual adjustment of post-processing setup for: (a) directional and (b) omnidirectional AUT. Lack of consistency between LoS (red) and non-LoS (black) peaks at different center frequencies (—, - -), (•••) hinders determination of suitable bandwidth based on visual inspection of the response prior to measurements.

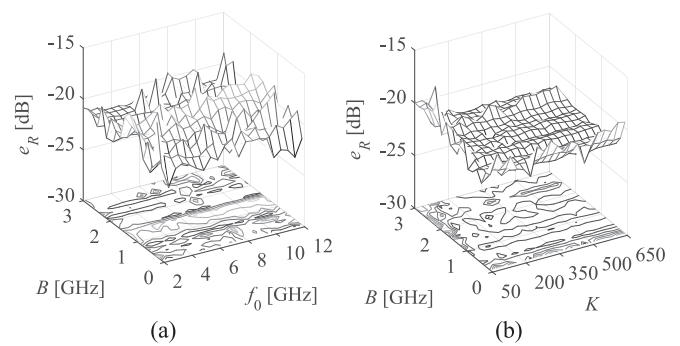


Fig. 3. Visualization of error  $e_R$  (see Section 2.3) between corrected non-anechoic responses and AC-based measurements as a function of: (a) bandwidth and center frequency ( $K = 201$ ) and (b) bandwidth and frequency sweep granularity ( $f_0 = 3$  GHz). The correction results have been obtained using method of Section 3.1 with composite kernel.

optimization of algorithm-specific parameters. When evaluation of far-field radiation patterns is considered, it is desired to formulate the problem as a curve-fitting task. As already mentioned, the main assumption behind post-processing of non-anechoic experiments is lack of AC-based AUT responses. Having that in mind the objective function can be formulated so as to minimize the discrepancy between the refined non-anechoic responses and their corresponding EM simulation characteristics. Unfortunately, EM models are often subject to multiple simplifications that do not fully reflect the behavior of prototype designs. Performance of the latter is also altered by a range of uncertainties resulting from, e.g., manufacturing tolerances, manual assembly of connectors (including adjustment of location and soldering), inconsistent positioning of the antennas, or the test setup itself. The consequence is that the discrepancies between simulated responses and corrected measurements are often substantial which might hinder optimization. Here, the mismatch between EM and corrected responses is reduced based on uniform scaling of the former performed in the course of the setup optimization. Such approach re-formulates the problem so as to retain the desired shape of the response while suppressing the effects of level-over-angle discrepancies on the outcome of correction. Additional challenge is related to the mentioned complexity of functional landscape, which puts stringent requirements upon numerical methods that can be used for optimization (cf. Fig. 3). Here, appropriate combination of setup parameters is sought as a result of derivative-free optimization [40,41].

Let  $\mathbf{x} = [B K]^T$  denote the setup for post-processing algorithm of choice (cf. Section 3). Then, let  $\mathbf{R}_c(f_0, \theta) = \mathbf{R}_c(\mathbf{x}, f_0, \theta) = \mathbf{R}_c(\mathbf{x})$  be the corrected response obtained for the given vector of hyperparameters  $\mathbf{x}$ . The goal of setup adjustment is to obtain  $\mathbf{x}^*$  for which  $\mathbf{R}_c$  provides approximation of the AC-based radiation pattern response with an acceptable fidelity. The problem is given as:

$$\mathbf{x}^* = \underset{\mathbf{x}}{\operatorname{argmin}}(e_R(\mathbf{R}_c(\mathbf{x}), \alpha(\mathbf{x})\mathbf{R}_s)) \quad (2)$$

where  $\mathbf{R}_s = \mathbf{R}_s(f_0, \theta)$  is the EM simulation data and  $e_R(\mathbf{R}_c(\mathbf{x})) = e_R(\mathbf{R}_c(\mathbf{x}), \mathbf{R}_0(\mathbf{x}))$ —here,  $\mathbf{R}_0(\mathbf{x}) = \alpha(\mathbf{x})\mathbf{R}_s$ —represents a similarity metric between the corrected and reference response  $\mathbf{R}_0$  expressed in terms of the root-mean-square-error:

$$e_R(\mathbf{R}_c(\mathbf{x})) = \left( \frac{1}{A} \sum_{a=1}^A (R_0(f_0, \theta_a) - R_c(\mathbf{x}, f_0, \theta_a))^2 \right)^{0.5} \quad (3)$$

It should be emphasized that, although  $\mathbf{R}_0$  in (3) refers to EM simulations when optimization of  $\mathbf{x}$  is considered, the parameter can also be used to denote antenna measurements performed in anechoic chamber. This is clearly indicated in Section 4 where numerical validation of the proposed framework is performed. The multiplicative component  $\alpha$  in

(2) ensures vertical scaling of the EM-based response in the course of the optimization process. It is extracted as a solution to the following least-squares problem:

$$\alpha(\mathbf{x}) = (\mathbf{R}_s^T \mathbf{R}_s)^{-1} \mathbf{R}_s^T \mathbf{R}_c(\mathbf{x}) \quad (4)$$

In practice, the scaling of EM responses in (3) is performed at each design  $\mathbf{x}$  obtained during minimization of (2). The rationale here is to ensure that the tuning process is oriented towards increasing the overall resemblance between the corrected and reference responses rather than matching their angle-specific amplitudes. Overall, the process allows to narrow-down the close-to-optimum setup and further exploit the search space to improve the responses. The proposed curve-fitting mechanism can be summarized as follows (see Fig. 4 for conceptual illustration):

1. For the given  $\mathbf{x}$ , and correction method of Section 3 obtain  $R_c(\mathbf{x})$ ;
2. Find uniform scaling coefficient  $\alpha(\mathbf{x})$  for  $R_s$  by solving (4);
3. Calculate  $R_0(\mathbf{x}) = \alpha(\mathbf{x})R_s$  and evaluate the error (3).

The above-outlined procedure is embedded into the optimization loop (2) in order to determine desirable setup for the correction algorithm of choice. It should be noted that, due to “dynamics” associated with scaling of reference responses, as well as non-differentiable character of the search space (cf. Fig. 3), minimization of (2) is challenging. Here, the task is performed using a pattern search algorithm outlined in Section 2.4 [40]. To mitigate the risk of getting stuck in poor local optimum, the optimization process is re-set from several starting points evenly selected within the design space.

A practical challenge concerning adjustment of bandwidth and frequency sweep is that the optimum values cannot be reliably determined *a priori*. The problem can be mitigated either by measuring the RA-AUT transmission over a wide bandwidth with a high granularity of points (useful e.g., for broadband structures), or by selecting relatively conservative bandwidth. The latter method might involve additional experiments when the optimized design is identified at the upper bound for one or more parameters. Here, broadband measurements are considered as they involve little overhead in terms of the time required for data gathering while ensuring that the required data points are obtained in one shot.

#### 2.4. Derivative-free optimization engine

Minimization of (2) is performed using a pattern search heuristic [40]. To ensure self-consistency, a brief description of the considered optimization engine is provided here. Pattern search is a local method that iteratively seeks for the optimum design,  $i = 0, 1, \dots, I$ , through

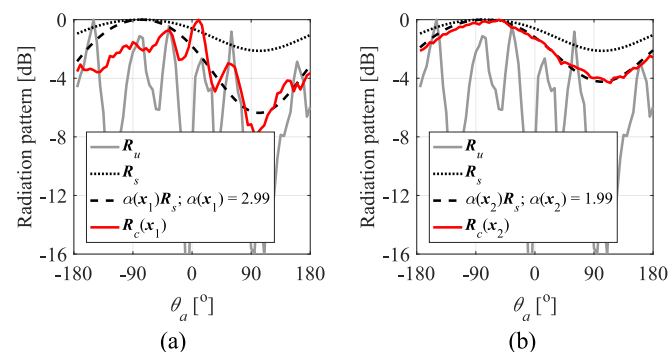


Fig. 4. Demonstration of curve-fitting mechanism based on omnidirectional antenna responses (normalized gain) at  $f_0 = 4$  GHz: (a) for  $\mathbf{x}_1$  setup and (b) for  $\mathbf{x}_2$  setup in the course of the tuning process. The role of  $\alpha(\mathbf{x})$  coefficient is to provide uniform vertical scaling of the EM simulation results (•••) so as to ensure that  $e_R$  error represents to shape-wise discrepancy between responses rather than their level-wise misalignment.

evaluation of candidate solutions around the best available design  $\mathbf{x}^{(i)}$  according to pre-determined rules. The routine used in this work embeds two mechanisms for identification of promising solutions, i.e., line and local search.

Line search involves evaluation of positive perturbations  $\mathbf{X} = \{\mathbf{x}_1, \dots, \mathbf{x}_d\}$ ,  $d = 1, \dots, D$ , around  $\mathbf{x}^{(i)}$  according to the given objective function  $U = \{U_1, \dots, U_d\}$ , where  $U_d = U(\mathbf{x}_d) = U(\mathbf{R}(\mathbf{x}_d))$  on a fixed grid that determines resolution of the optimization (here,  $D$  denotes the dimensionality of  $\mathbf{x}$ ). The perturbed designs are given as  $\mathbf{x}_d = \mathbf{x}^{(i)} + \mathbf{h}_d$ , where  $\mathbf{h}_d = [0 \dots q_d \dots 0]^T$ ; the sizes of perturbations w.r.t each dimension  $\mathbf{q} = [q_1 \dots q_d]$  are predefined. The objective function values of perturbed designs are used to determine the candidate design  $\mathbf{x}_l = \mathbf{x}^{(i)} + \delta$ , where  $\delta = \beta(|\mathbf{q}|/|\beta|)$  is the normalized search direction estimated from  $\beta = -(\mathbf{U} - \mathbf{U}^{(i)}) \div \mathbf{q}$  which is an approximation of negative gradient w.r.t.  $U^{(i)} = U(\mathbf{R}(\mathbf{x}^{(i)}))$  response (note that “ $\div$ ” denotes component-wise division). Since the optimization is performed on a grid, the candidate design  $\mathbf{x}_l$  must be rounded to the nearest discrete point before evaluation. Given that the objective function response for  $\mathbf{x}_l$  satisfies  $U_l < U^{(i)}$ , the design  $\mathbf{x}^{(i)} = \mathbf{x}_l$  is set along with  $U^{(i)} = U_l$  and the line search direction is adjusted as  $\delta = 2\delta$ . Otherwise, the design is discarded and algorithm reverts to local search mode.

In local search mode, the set  $\mathbf{X}_D = \{\mathbf{x}_{d+D}, \dots, \mathbf{x}_{2D}\}$  that contains negative perturbations to  $\mathbf{x}^{(i)}$  given as  $\mathbf{x}_{D+d} = \mathbf{x}^{(i)} - \mathbf{h}_d$  is generated and its components are evaluated to obtain  $U_D = \{U_{D+1}, \dots, U_{D+d}\}$ , where  $U_{D+d} = U(\mathbf{x}_{D+d})$ . If minimum value of the combined objective functions  $U_t = \min(\{U, U_D\})$  satisfies  $U_t < U^{(i)}$ , then  $\mathbf{x}_t \in \{\mathbf{X}, \mathbf{X}_D\}$  that corresponds to  $U_t$  is selected as the new best design—i.e.,  $\mathbf{x}^{(i+1)} = \mathbf{x}_t$  and  $U^{(i+1)} = U_t$ —and the algorithm again switches to line search mode. Otherwise, the perturbations are scaled down as  $\mathbf{q} = \mathbf{q}/Q$  and local search step is repeated. The algorithm is terminated when either the maximum number of iterations  $I$  is reached, or  $|\mathbf{q}| < \epsilon$ . The method can be summarized as follows (see Fig. 5 for conceptual illustration):

1. Set  $i = 0$ ,  $\mathbf{x}^{(i)} = \mathbf{x}_0$ ,  $\mathbf{q}$ , and  $Q$ ; evaluate  $\mathbf{x}^{(i)}$  to obtain  $U^{(i)}$ ;
2. Generate  $\mathbf{X}$  according to given perturbations  $\mathbf{q}$  and obtain  $U$ ;
3. Calculate search direction  $\delta$ , set  $\mathbf{x}_l = \mathbf{x}^{(i)} + \delta$  and obtain  $U_l$ ;
4. If  $U_l < U^{(i)}$ , set  $\mathbf{x}^{(i+1)} = \mathbf{x}_l$ ,  $U^{(i+1)} = U_l$ ,  $\delta = 2\delta$  and go to Step 8; otherwise go to Step 5;
5. Generate  $\mathbf{X}_D$  according to  $\mathbf{q}$ , obtain  $U_D$ , and find  $\mathbf{x}_t$  for which  $U_t = \min(\{U, U_D\})$ ;
6. If  $U_t < U^{(i)}$ , set  $\mathbf{x}^{(i+1)} = \mathbf{x}_t$ ,  $U^{(i+1)} = U_t$  and go to Step 8; otherwise scale down perturbations as  $\mathbf{q} = \mathbf{q}/Q$  and go to step 7;
7. If  $|\mathbf{q}| < \epsilon$ , set  $\mathbf{x}^* = \mathbf{x}^{(i)}$  and END; otherwise set  $\mathbf{x}^{(i+1)} = \mathbf{x}^{(i)}$ ,  $U^{(i+1)} = U^{(i)}$ ;
8. Set  $i = i + 1$ . If  $i < I$  go to Step 2; otherwise set  $\mathbf{x}^* = \mathbf{x}^{(i)}$  and END.

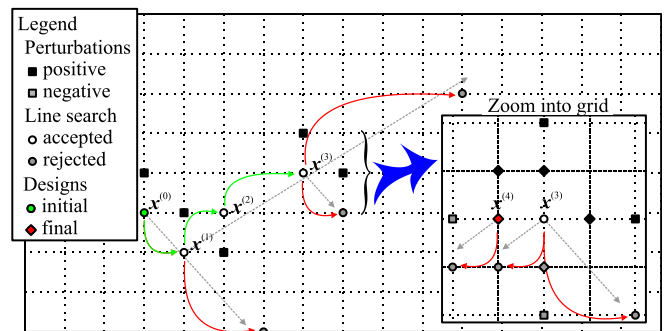


Fig. 5. Conceptual illustration of derivative-free optimization using pattern-search heuristic. Gray arrows denote descent directions estimated from positive perturbations. Green and red arrows represent line search jumps to accepted and rejected designs. Inset shows a zoom into grid with increased granularity (i.e.,  $\mathbf{q} = \mathbf{q}/Q$ ), with highlight on perturbations in reduced grid (◆). Design  $\mathbf{x}^* = \mathbf{x}^{(4)}$  is obtained upon termination of the algorithm.

The vector  $\mathbf{x}^*$  is the final design obtained using the algorithm. To enforce feasibility of the optimization, candidate designs from  $\mathbf{X}$  and/or  $\mathbf{X}_D$  that exceed the lower/upper bounds  $l_b/u_b$  of the search space are discarded. Note that evaluation of designs in the course of optimization is performed here using (3) as objective function. The user-defined parameters are set to  $Q = 1.5$ ,  $I = 50$ , and  $\varepsilon = 0.05$ , respectively. For more comprehensive discussion on the considered algorithm and its applications, see [40,41].

### 2.5. Summary of the framework

The proposed framework for automatic adjustment of correction setup involves a series of optimizations re-set from pre-determined designs. Let  $\mathbf{X}_0 = \{\mathbf{x}_{0,1}, \dots, \mathbf{x}_{0,p}\}$  be a set of  $p = 1, \dots, 2D + 1$  setup vectors generated using a star-distribution design of experiments and scaled according to the lower and upper bounds  $l_b$  and  $u_b$  as  $l_{b,1} = l_b + \mathbf{d}_0$  and  $u_{b,1} = u_b - \mathbf{d}_0$  [54]. Here,  $\mathbf{d}_0 = (u_b - l_b)/5$  is used. The bounds  $l_{b,1}/u_{b,1}$  for  $\mathbf{X}_0$  are reduced w.r.t.  $l_b/u_b$  so as to ensure that the initial designs are determined away from the search space edges. The framework can be summarized as follows (see Fig. 6 for conceptual illustration):

1. Set  $p = 1$ , define  $l_b$ ,  $u_b$ , initialize  $\mathbf{X}^* = \{\}$ ,  $\mathbf{E}_{R^*} = \{\}$ , and generate  $\mathbf{X}_0$ ;
2. Set  $\mathbf{x}^{(0)} = \mathbf{x}_{0,p}$  and find  $\mathbf{x}_p^*$  by solving (2) using the correction algorithm of choice (cf. Section 3) and the optimization engine of Section 2.4;
3. Add  $\mathbf{x}_p^*$  and its corresponding  $e_{R,p}^*$  response to  $\mathbf{X}^*$  and  $\mathbf{E}_{R^*}$  sets;
4. If  $p < 2D + 1$  set  $p = p + 1$  and go to Step 2; otherwise set  $\mathbf{x}^* = \mathbf{x}_\mu^*$  and END;

Note that  $\mu$  is the index of the design from  $\mathbf{X}^*$  set that corresponds to  $e_{R,\mu} = \min\{\mathbf{E}_{R^*}\}$ . The design  $\mathbf{x}^*$  obtained by solving (2) is considered as optimal setup for the correction algorithm of choice at the given frequency of interest  $f_0$ . The proposed routine can be considered generic as it is independent from the selected post-processing method (cf. Section 3). The computational cost of the procedure is negligible when compared to the time-involvement associated with acquisition of RA-AUT transmission in non-anechoic environments.

### 3. Multi-frequency post-processing

Multi-frequency post-processing algorithms fall into two main categories that include analysis either in time or frequency domains. The proposed automatic tuning framework, owing to generic

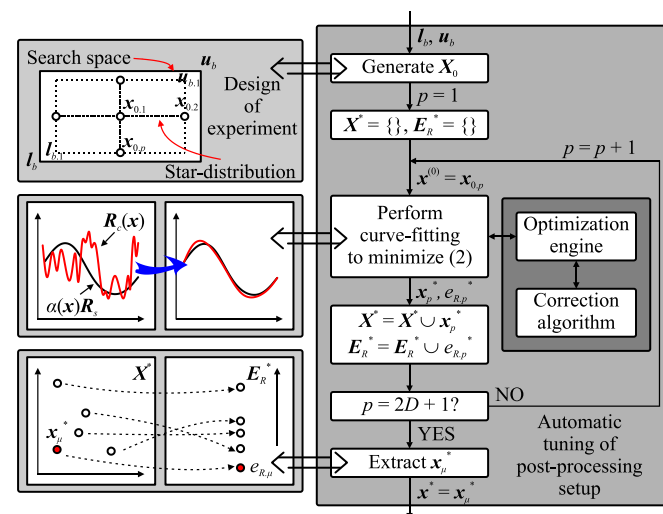


Fig. 6. A block diagram of the framework for automating adjustment of post-processing setup with highlight on its key components.

implementation, supports correction of signals transmitted between the RA-AUT system components using both classes of methods. To ensure that the paper is self-contained, a brief discussion of three routines, i.e., time-gating, Morlet, and matrix-pencil-based post-processing is provided. The mentioned schemes can be executed within the general algorithm of Section 2.1. Furthermore, correction performance of the methods is subject to appropriate tuning of both bandwidth  $B$  and the number of frequency points  $K$  (associated with the  $\delta\omega$  step). Numerical results and discussions are provided in Sections 4 and 5, respectively.

### 3.1. Time-gating correction

Time-gating method (TGM) approximates the amplitude of RA-AUT transmission as a result of three-step procedure where the original response is: (i) converted to the time-domain, (ii) modified using a suitable kernel, and (iii) transformed back to the frequency response [10]. The algorithm is executed separately at each  $\theta_a$ ,  $a = 1, \dots, A$ , angle (cf. Section 2.1). Let an  $N$ -point impulse response—obtained from the frequency-based transmission using an inverse Fourier transform  $\mathcal{F}^{-1}(\bullet)$ —be given as:

$$T_u(t, \theta_a) = \mathcal{F}^{-1}(\mathbf{R}_u(\omega, \theta_a), N) \quad (5)$$

The time-domain sweep is  $\mathbf{t} = [t_1 \dots t_N]^T = \delta\mathbf{t}\mathbf{M}$  where  $\mathbf{M} = -(0.5N + 1) + [1 \dots N]^T$  and  $N = 2^{\lceil \log_2(K) \rceil + 3}$  (note that  $N$  is even;  $\lceil \bullet \rceil$  represents a round-up to an integer). Now, let  $t_{i,1}, t_{i,2} \in \mathbf{t}$  ( $t_1 \leq t_{i,1} < t_{i,2} \leq t_N$ ) represent the experience-derived interval for the kernel function and  $i_1, i_2$  ( $1 \leq i_1 < i_2 \leq N$ ) denote its indices. The kernel is of the form  $\mathbf{T}_k = \mathbf{T}_k(\mathbf{t}, \mathbf{m}) = [\mathbf{O}_1 \mathbf{T}_w(\mathbf{m}) \mathbf{O}_2]^T$  with  $\mathbf{O}_1$  and  $\mathbf{O}_2$  being  $i_1 - 1$  and  $N - i_2$  long vectors of zeros, and  $\mathbf{m} = [1 \dots i_2 - i_1] - 1$ ;  $\mathbf{T}_w$  is typically in the form of box (rectangular), or Hann functions [42]. The former is given as  $\mathbf{T}_w(\mathbf{m}) = \mathbf{1}_a$  with  $\mathbf{1}_a$  being  $i_2 - i_1$  long vector of ones. Hann function is defined as  $\mathbf{T}_w(\mathbf{m}) = 0.5 - 0.5\cos(2\pi\mathbf{m})$ . It should be reiterated that determination of  $t_{i,1}$  to  $t_{i,2}$  interval for TGM is up to the user. Alternatively, the kernel that represents a combination of functions can be derived based on evaluation of the impulse response [12]. Let  $t_{b,1}$  and  $t_{b,2}$  represent the time instances at which the amplitude of the LoS peak crosses 5 % and 40 % of its maximum height (at raise) and let  $t_{b,3}$  and  $t_{b,4}$  correspond to 40 % and 5 % of the height at decline, respectively, whereas  $\mathbf{b} = [b_1 \ b_2 \ b_3 \ b_4]$  ( $1 \leq b_1 < b_2 < b_3 < b_4 \leq N$ ) represent their corresponding indices. The kernel is of the form  $\mathbf{T}_k = \mathbf{T}_k(\mathbf{t}, \mathbf{b}) = [\mathbf{O}_3 \mathbf{T}_{w,1}(\mathbf{m}_{12}) \mathbf{T}_{w,2}(\mathbf{m}_{23}) \mathbf{T}_{w,3}(\mathbf{m}_{34}) \mathbf{O}_4]^T$ , where  $\mathbf{T}_{w,1}(\mathbf{m}_{12}) = 0.42 - 0.5\cos(2\pi\mathbf{m}_{12}/(2 \ m_{12})) + 0.08\cos(4\pi\mathbf{m}_{12}/(2 \ m_{12}))$ ,  $\mathbf{T}_{w,2}(\mathbf{m}_{23}) = \mathbf{1}_{23}^T$ , and  $\mathbf{T}_{w,3}(\mathbf{m}_{34}) = 0.54 - 0.46\cos(2\pi\mathbf{m}_{34}/(2 \ m_{34}))$ . Note that  $\mathbf{m}_{12} = b_2 - b_1$ ,  $\mathbf{m}_{23} = b_3 - b_2$ , and  $\mathbf{m}_{34} = b_4 - b_3$ , whereas  $\mathbf{m}_{12} = [0 \dots \mathbf{m}_{12}]$ ,  $\mathbf{m}_{34} = [0 \dots \mathbf{m}_{34}]$  and  $\mathbf{1}_{23}^T$  is  $\mathbf{m}_{23} + 1$  element vector of ones. Furthermore,  $\mathbf{O}_3$  and  $\mathbf{O}_4$  are  $b_1 - 1$  and  $N - b_4$  vectors of zeros.

The corrected time-domain response is  $\mathbf{T}_c(\mathbf{t}, \theta_a) = \mathbf{T}_u(\mathbf{t}, \theta_a) \circ \mathbf{T}_k$ , where “ $\circ$ ” represents a Hadamard product, and  $\mathbf{T}_k$  denotes the kernel of choice (i.e., either rectangular, Hann, or composite). Next, the modified time-domain response is converted back to frequency  $\boldsymbol{\Omega} = \delta\omega\mathbf{M} - B + f_0$  using  $N$ -point Fourier transform:

$$\mathbf{R}_c(\boldsymbol{\Omega}, \theta_a) = \mathcal{F}(\mathbf{T}_c(\mathbf{t}, \theta_a), N) \quad (6)$$

Finally,  $\mathbf{R}_c(\omega, \theta_a)$ —that contains  $K \leq N$  frequency points around  $f_0$  ( $\omega \in \boldsymbol{\Omega}$ )—is extracted from  $\mathbf{R}_c(\boldsymbol{\Omega}, \theta_a)$ . For more detailed discussion on conventional time-gating post-processing, see [9,10,12,18].

### 3.2. Morlet-based post-processing

The basic concept behind Morlet-based correction is similar to TGM. However, the algorithm embeds mechanism for angle-wise estimation of the kernel with respect to local changes of the RA-AUT distance [39]. The profile extraction is executed at all  $\theta$  angles as a separate step before post-processing. The algorithm is as follows. Let  $\mathbf{P}_u = \mathbf{P}_u(\mathbf{t}, \theta_a) = \mathbf{T}_u \circ \mathbf{T}_u^H$  be the power response, where  $\mathbf{T}_u$  is obtained using (5); “ $H$ ” denotes a

Hermitian transpose. Owing to being smooth functions of time, power characteristics can be used to identify LoS peaks. For one-shot measurements (as considered in this work) the delay profile  $\mathbf{d}_c = [d_{c,1} \dots d_{c,a}]$  is extracted as follows [39]:

1. Set  $t_l = 0$ ,  $t_h = \delta t(0.5N - 1)$ , and  $\gamma = 1$ ;
2. Find  $d_{u,a} = \text{argmax}(\mathbf{P}_u(t_u, \theta_a))$ ,  $t_u = [t_l \dots t_h]$  ( $t_u < \mathbf{t}$ ) for each  $\theta_a$  angle and construct  $\mathbf{d}_u = [d_{u,1} \dots d_{u,a}]$ ;
3. If  $\gamma = 1$ , find  $d_0 = \min(\mathbf{d}_u)$ , set  $t_l = d_0 - 3h_0$ ,  $t_h = d_0 + 3h_0$ ,  $\gamma = 2$  and go to Step 2; otherwise go to Step 4.
4. Apply median filter and moving average to obtain  $\mathbf{d}_c$  from  $\mathbf{d}_u$ .

The parameter  $h_0$  denotes half-prominence of the peak (i.e., its width at half of height). The median filter is given as [39]:

$$d_{c,a} = \begin{cases} (d_{u,a-1} + d_{u,a+1})/2, & \text{when } d_{u,a} \geq M(\mathbf{d}_u) + 2\sigma(\mathbf{d}_u) \\ (d_{u,a-1} + d_{u,a+1})/2, & \text{when } d_{u,a} \leq M(\mathbf{d}_u) - 2\sigma(\mathbf{d}_u) \\ d_{u,a}, & \text{otherwise} \end{cases} \quad (7)$$

Note that  $M(\bullet)$  and  $\sigma(\bullet)$  denote median and standard deviation, respectively. As already mentioned, the extracted vector of delays  $\mathbf{d}_c = [d_{c,1} \dots d_{c,a}]$  is used to center the kernels around LoS peaks. The Morlet wavelet is a combination of exponential function with Gaussian curve of the form [39]:

$$T_k(t, \theta_a) = \exp\left(2\left(j\pi f_0(t - d_{c,a}) - (\pi f_0(t - d_{c,a})w^{-1})^2\right)\right) \quad (8)$$

The parameter  $w$  represents the number of cycles that affect confinement of the LoS peak within the wavelet. Its specific value is determined by solving:

$$w^* = \text{argmin}(U(w, f_0, \theta_0)) \quad (9)$$

with  $U$  being of the form:

$$U(w, f_0, \theta_0) = \sum (\mathbf{P}_e(t, \theta_0) - \mathbf{G}(w, t, \theta_0, f_0))^2 \quad (10)$$

where  $\mathbf{P}_e$  is a normalized power response at  $\theta_0$  angle that corresponds to the  $d_0$  delay. The second component of the objective function is given as:

$$\mathbf{G}(w, t, \theta_0, f_0) = \exp\left(-2\left((\pi f_0(t - d_0))w^{-1}\right)^2\right) \quad (11)$$

Minimization of (10) ensures that useful part of the RA-AUT response is tightly confined by the wavelet. The computational cost of (9) is negligible as the process is performed only at  $\theta_0$  using already processed responses. Upon extraction of  $w$ , the kernel is used to modify uncorrected impulse response which is then converted back to the frequency domain as in (6). Finally,  $\mathbf{R}_c(\omega, \theta_a)$  is extracted from  $\mathbf{R}_c(\Omega, \theta_a)$ . More detailed discussion on Morlet-based post-processing can be found in [39,43].

### 3.3. Matrix-pencil algorithm

The last considered method involves correction in the frequency domain. The matrix-pencil algorithm (MPA) approximates RA-AUT transmission using the following composition of basis functions [44]:

$$\mathbf{R}(\omega, \theta_a) = \sum_{m=1}^M r_m z_m^{\kappa} \quad (12)$$

The vector  $\kappa = [1 \dots K]^T - 1$ , whereas  $z_m$  and  $r_m$  ( $m = 1, \dots, M$ ) represent complex exponential functions and residues. Let  $\mathbf{H} = \mathbf{H}(\omega, \theta_a)$  be a Hankel matrix constructed from the uncorrected RA-AUT responses [44]:

$$\mathbf{H}(\omega, \theta_a) = \begin{bmatrix} R_u(\omega_1, \theta_a) & R_u(\omega_2, \theta_a) & \dots & R_u(\omega_L, \theta_a) \\ R_u(\omega_2, \theta_a) & R_u(\omega_3, \theta_a) & \dots & R_u(\omega_{L+1}, \theta_a) \\ \vdots & \vdots & \ddots & \vdots \\ R_u(\omega_{K-L-1}, \theta_a) & R_u(\omega_{K-L}, \theta_a) & \dots & R_u(\omega_{K-1}, \theta_a) \end{bmatrix} \quad (13)$$

Here,  $L \in [M; K - M]$  (note that  $M \ll K$ ) is a so-called pencil parameter. Also, let  $\mathbf{H} = \mathbf{U}\mathbf{\Psi}\mathbf{V}^H$ , where  $\mathbf{V} = \mathbf{V}(\omega, \theta_a) = \mathbf{H}^H\mathbf{H}$  and  $\mathbf{U} = \mathbf{U}(\omega, \theta_a) = \mathbf{H}\mathbf{H}^H$  comprise eigenvectors, while  $\mathbf{\Psi} = \mathbf{\Psi}(\omega, \theta_a)$  denotes a diagonal matrix containing singular values of  $\mathbf{H}$ . The exponential functions of  $\mathbf{z} = [z_1 \dots z_m]$  are obtained as eigenvectors of  $\mathbf{Y}_1^+ \mathbf{Y}_2$  (the symbol “+” denotes a Moore-Penrose inverse), where  $\mathbf{Y}_1 = \mathbf{U}\mathbf{\Psi}_M\mathbf{V}_1^H$  and  $\mathbf{Y}_2 = \mathbf{U}\mathbf{\Psi}_M\mathbf{V}_2^H$ ;  $\mathbf{\Psi}_M$  consists of all but the first and last row of  $\mathbf{V}_M$ . The latter is constructed from all rows and first  $M$  columns of  $\mathbf{V}$ . The vector of residuals  $\mathbf{r} = [r_1 \dots r_m]$  is obtained as a solution to the least-squares problem given as  $\mathbf{r} = \mathbf{Z}^+ \mathbf{R}(\omega, \theta_a)$ , where  $\mathbf{Z}$  is the Vandermonde matrix constructed from  $\mathbf{z}$  [44].

Contrary to methods based on time-domain post-processing, MPA embeds mechanism for automatic identification of LoS signals within the RA-AUT system. Let  $\mathbf{t}_a = [t_1 \dots t_m]$  be the vector of delays at  $\theta_a$  angle, where  $m$ th component is of the form:

$$t_{a,m} = \tan^{-1}\left(\frac{\text{Re}(z_m)/\text{Im}(z_m)}{(\delta\omega \cdot 2\pi)}\right) \quad (14)$$

The corrected response is obtained as  $\mathbf{R}_c(\omega, \theta_a) = r_{\kappa} z_{\kappa}$ , where  $\kappa$  represents an index for which  $t_{a,m} = \min(\mathbf{t}_a)$ . Similarly as for the remaining methods, the algorithm is executed separately at all  $\theta_a$  angles. For more, comprehensive discussion on MPA, see [9,44,45].

## 4. Correction results

The proposed framework for automatic tuning of post-processing settings has been demonstrated using three antennas shown in Fig. 7. These include Vivaldi radiator, compact monopole, and quasi-Yagi structure [20]. The experiments have been conducted in two non-anechoic offices with dimensions of  $8.4 \times 4.5 \times 3.1 \text{ m}^3$  (site A) and  $5.5 \times 4.5 \times 3.1 \text{ m}^3$  (site B), respectively. The considered environments (see Fig. 8) are deemed unsuitable for far-field experiments due to lack of radiation absorbing materials, no isolation from the external EM noise, as well as a number of potential obstacles, and/or reflectors for transmitted signals (furniture, whiteboards, computers, etc.). The measurements have been performed using an in-house mobile positioning towers (see Fig. 1 for schematic diagram) [46]. The angular resolution of AUT is set to  $5^\circ$  (72 measurements are required to cover  $360^\circ$  radiation pattern in a single elevation plane). For all of the considered correction routines, automatic adjustment of setup is oriented towards identification of optimum  $B$  and  $K$  (cf. Section 2.3). The lower and upper bounds on the parameters are set to  $\mathbf{l}_b = [0.1 \ 51]^T$  and  $\mathbf{u}_b = [3.5 \ 651]^T$ , respectively. For each experiment, the Vivaldi structure is used as the reference antenna. Maximum number of iterations for the pattern search algorithm [40,41], is set to 50 in order to ensure low cost of hyper-parameters adjustment process. It should be noted that LoS/NLoS delays—estimated based on manual measurement of the RA-AUT distance, as well as the first expected reflected signal—for the first and second site are 6.7 ns/10.4 ns and 6.7 ns/14.9 ns, respectively. Please note that the obtained time delay (between NLoS and LoS signals) for the first, larger room is smaller than for the second site due to the reflective sheet positioned on the ceiling between the two antenna structures.

Performance of the proposed framework has been compared against rule-of-thumb-based approaches from the literature that include: (i) determination of minimum bandwidth  $B$  in relation to the size of antenna aperture with a fixed number of frequency points  $K$ , (ii) estimation of  $B$  and  $K$  for the purpose of echo cancellation, (iii) fixed selection of minimum  $B$  and  $K$ , and (iv) determination of  $B$  and  $K$  in accordance to functional landscape of  $e_R$  error (see Section 2.3). It is worth noting that, contrary to time-domain methods of Sections 3.1 and 3.2, MPA introduces two additional parameters that have not been optimized (for consistency). These include number of exponentials and pencil parameter that have been set—based on the literature [44]—to  $L = [K/3 + 0.5]$  and  $M = 2$ , respectively. The post-processing performance is evaluated in terms of root-mean-square-error (3) calculated with respect to

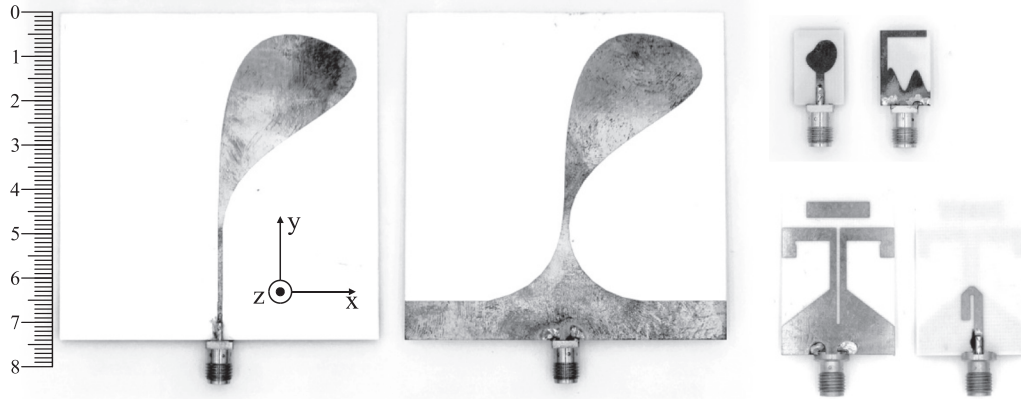


Fig. 7. In-scale photographs (scale bar unit: mm) of antenna prototypes used for measurements: Vivaldi (left), compact monopole (top right), and quasi-Yagi structure (bottom right) [38,46]. Note that Vivaldi radiator is used as RA for all of the experiments.

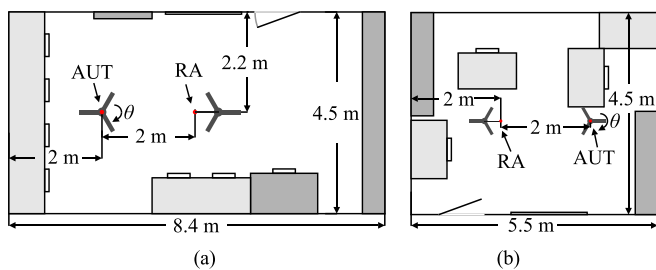


Fig. 8. Schematic diagrams of test sites used for experiments: (a) room A and (b) room B. Light- and dark-shade gray rectangles denote short and tall furniture. Red dots represent RA and AUT locations on positioning towers.

the AC-based responses ( $\mathbf{R}_0 = \mathbf{R}_{AC}$ ; cf. Section 2.3). Overall, a total of 1250 experiments spanned over two test sites, five approaches (setups) to determine hyperparameters, five versions of time- and frequency-domain correction algorithms for 25 unique frequencies of interest divided among three antenna structures (11 for Vivaldi and 7 each for monopole and quasi-Yagi) have been performed. A detailed discussion of the results is provided in Section 5.

#### 4.1. Test site A

For the test site of Fig. 8(a), the radiation performance figures of considered antennas have been characterized (in  $yz$ -plane) at the following sets of frequency points, i.e.  $f_0 = \{2, 3, 4, 5, 6, 7, 8, 9, 10, 11, 12\}$  GHz for Vivaldi,  $f_0 = \{3.5, 4, 4.5, 5, 5.5, 6, 6.5\}$  GHz for monopole and  $f_0 = \{4, 4.5, 5, 5.5, 6, 6.5, 7\}$  GHz for quasi-Yagi. The performance has been evaluated using five post-processing methods: (i) TGM with rectangular, (ii) Hann, and (iii) composite kernels, (iv) Morlet-based approach, and (v) MPA. Additionally, five different setups for hyperparameters  $B$  and  $K$  were used, including four rule-of-thumb-based methods (setups 1 to 4) and the proposed framework.

The first setup involved determining the minimum bandwidth  $B$  based on the antenna aperture size, with a dedicated number of frequency points  $K$  as outlined in [38]. The bandwidth was set to 1 GHz for the Vivaldi radiator, 3 GHz for the monopole, and 2 GHz for the quasi-Yagi. The number of frequency points was fixed at a minimum value of  $K = 201$  for each structure, resulting in a total of three sets of hyperparameters.

For the second setup, sufficiently wide bandwidth is suggested to resolve multipath components, facilitating the identification and cancellation of echoes, while the selection of frequency points has to ensure the avoidance of time-domain aliasing [9]. For FFT-based

methods, the bandwidth is determined as the ratio of 10 to the time delay (between the direct LoS signal and the first echo), whereas for matrix-pencil method, the ratio is set to 1. The number of frequency points is calculated as the ratio of  $B$  to the frequency step size  $df = 5$  MHz [9]. Consequently, the setup established two distinct hyperparameter sets for all antenna structures:  $B = 2.7$  GHz,  $K = 541$  for TGM and Morlet methods, as well as  $B = 0.27$  GHz,  $K = 53$  for MPA.

The third setup is derives appropriate  $B$  and  $K$  for measurements based on recommendations formulated for reverberating enclosures [10]. Similarly to [9], the minimum bandwidth was given as the ratio of 1 to the time delay, ensuring adequate separation between the direct signal and its reflections (cf. Section 2.2). For improved accuracy, the bandwidth was fixed at 1 GHz, with the number of frequency points determined by the ratio of  $B$  to the frequency step size  $df = 3$  MHz. Therefore, for all antenna structures and all post-processing methods, the setup was set to  $B = 1$  GHz,  $K = 333$  (i.e., a single set of hyperparameters).

The fourth setup involves identification of local minima in the functional landscape of  $e_R$  error between the corrected non-anechoic responses and EM simulation-based measurements, visualized as a function of  $B$  and  $K$ . The reference frequencies are set to  $f_0 = 7$  GHz for Vivaldi,  $f_0 = 6.5$  GHz for monopole and  $f_0 = 5.5$  GHz for quasi-Yagi. The minima are evaluated independently for each post-processing method, resulting in 15 distinct sets of hyperparameters (3 antennas  $\times$  5 methods).

Finally,  $B$  and  $K$  are determined based on the guidelines from Section 2.3. To effectively illustrate the core findings, a selection of representative tables and plots has been provided to manage the extensive volume of data generated throughout the study. This subset has been carefully curated to emphasize the most relevant patterns and outcomes, ensuring clarity without overwhelming the discussion with exhaustive data.

Table 1 presents the results obtained for MPA correction of the Vivaldi antenna, including the optimized  $K$  and  $B$  at each frequency. In the considered setup, the hyperparameters are specifically tailored to the frequency of interest, the antenna type, the correction method, and the test site. In contrast, setups 1 and 4 follow rule-of-thumb approaches, with  $\{K, B\}$  configurations of  $\{201, 1 \text{ GHz}\}$ , and  $\{311, 1.7 \text{ GHz}\}$ , respectively. One should reiterate that setups 2 and 3 are set the same for all considered antennas and have been defined above. Across the selected frequency points, the MP method with optimized parameters achieves lower or comparable error rates w.r.t. methods with conservative setup of variables. The correction performance averaged across the considered frequency points  $\mu_{eR}$  corresponds to  $-22.6$  dB for the optimized parameters and varies from  $-11.9$  dB to  $-21.21$  dB for the benchmark setups. It should also be noted that the presented approach

**Table 1**  
Vivaldi – optimized  $B$  and  $K$  for the MPA.

Proposed framework				Setup 1	Setup 2	Setup 3	Setup 4
$f_0$ [GHz]	$K$	$B$ [GHz]	$e_R^s$ [dB]	$e_R^s$ [dB]	$e_R^s$ [dB]	$e_R^s$ [dB]	$e_R^s$ [dB]
2	209	1.02	-17.00	-17.14	-8.34	-17.16	-13.96
3	207	0.54	-23.50	-21.34	-6.83	-24.39	-24.25
4	209	0.58	<b>-30.30</b>	-19.62	-9.42	<b>-31.27</b>	-27.00
5	265	0.88	-22.30	-22.12	-7.31	-22.12	-20.46
6	209	0.17	-19.30	-18.88	-12.01	-18.84	-19.05
7	261	2.10	-23.90	-15.15	-12.67	-15.11	-24.48
8	251	1.03	-22.50	-22.62	-17.83	-17.11	-23.10
9	217	0.78	-22.80	-23.45	-11.77	-15.87	-21.65
10	371	0.78	-21.80	-21.93	-13.30	-21.84	-20.19
11	409	1.63	-24.40	-22.36	-17.88	-22.50	-24.30
12	161	1.06	-20.70	-20.43	-13.49	-20.28	-14.86
$\mu_{eR}(\mathbf{R}_c(f_0, \theta))$			<b>-22.60</b>	-20.46	-11.90	-20.59	-21.21
$\sigma_{eR}(\mathbf{R}_c(f_0, \theta))$			3.34	2.55	3.76	4.64	4.07

$^s e_R = e_R(\mathbf{R}_c(f_0, \theta))$ ; Colormap: green – worst, red – best; Bold font: best average result.

offers relatively low standard deviation  $\sigma_{eR}$  of 3.3 dB. It is worth noting that, while the overall performance of MPA correction with optimized parameters is better compared to the rule-of-thumb-based setups, at selected benchmark settings, the latter outperform the correction with automatically determined parameters by 0.2 dB to 1 dB in terms of  $e_R$ . Overall, the results of Table 1 indicate that the presented framework offers competitive performance and acceptable deviation of the averaged results (especially when compared against conventional methods) while not relying on engineering experience for performance tuning.

Table 2 presents MPA correction for non-anechoic measurements of the monopole antenna. Setups 1 and 4 employ  $\{K, B\}$  parameters—determined using rules-of-thumb—of  $\{201, 3 \text{ GHz}\}$ , and  $\{231, 3.1 \text{ GHz}\}$ , respectively. Similarly as for Vivaldi, MPA method with optimized parameters exceeds conventional setups in terms of averaged correction performance. The obtained  $\mu_{eR}$  error corresponds to  $-28.8 \text{ dB}$ , whereas for remaining setups it varies from  $-6.9 \text{ dB}$  to  $-28.4 \text{ dB}$ . As it comes to standard deviation, the proposed approach offers comparable performance to setups 3 and 4. Although, the parameter is much lower for setups 1 and 2, the corresponding average  $e_R$  errors do not exceed  $-10 \text{ dB}$  which suggests that they are of no practical use for the given antenna and test site (at least when correction is performed using MPA).

The results obtained for the quasi-Yagi antenna, gathered in Table 3, also indicate that MPA adjusted using the presented framework outperforms benchmark setups (using  $\{201, 2 \text{ GHz}\}$ , and  $\{271, 3.3 \text{ GHz}\}$  for setup 1 and 4, respectively) in terms of  $\mu_{eR}$  error. The averaged error for automatic setup amounts to  $-22.2 \text{ dB}$ , and varies from  $-6.1 \text{ dB}$  to  $-20.3 \text{ dB}$  for rule-of-thumb setups. As it comes to standard deviation, the framework generates responses with the lowest value of 1.8 dB (among the useful results). Again, for setups 1 and 2, the parameter is around a much lower value of 1 dB, yet the low deviation is associated with poor performance.

Table 4 demonstrates applicability of the proposed framework for post-processing of non-anechoic measurements using the methods of

**Table 2**  
Monopole – optimized  $B$  and  $K$  for the MPA.

Proposed framework				Setup 1	Setup 2	Setup 3	Setup 4
$f_0$ [GHz]	$K$	$B$ [GHz]	$e_R^s$ [dB]	$e_R^s$ [dB]	$e_R^s$ [dB]	$e_R^s$ [dB]	$e_R^s$ [dB]
3.5	307	3.16	-30.40	-7.42	-5.33	-27.27	-30.73
4.0	311	1.32	-31.68	-7.80	-7.61	<b>-31.57</b>	-29.16
4.5	259	3.19	-29.20	-6.38	-8.30	-24.56	-28.91
5.0	279	3.31	-24.57	-7.97	-5.37	-23.53	-24.26
5.5	239	3.47	-26.31	-8.30	-9.64	-23.92	-25.36
6.0	425	2.10	-29.84	-9.10	-7.27	-27.57	-29.63
6.5	355	2.91	-29.39	-9.75	-4.69	-24.25	<b>-30.53</b>
$\mu_{eR}(\mathbf{R}_c(f_0, \theta))$			<b>-28.77</b>	-8.10	-6.89	-26.10	-28.37
$\sigma_{eR}(\mathbf{R}_c(f_0, \theta))$			2.47	1.10	1.81	2.91	2.54

$^s e_R = e_R(\mathbf{R}_c(f_0, \theta))$ ; Colormap: green – worst, red – best; Bold font: best average result.

Section 3. The obtained results indicate that for all but (i) algorithm, the average  $e_R$  error for the Vivaldi antenna—evaluated over the frequency range from 2 GHz to 12 GHz—is below  $-20 \text{ dB}$ . However, given rudimentary character of method (i), its low performance is expected. As it comes to algorithms (ii)-(v), when coupled with the framework, the maximum discrepancy between the obtained errors for the considered antenna amounts to only 1.2 dB. It should be noted that the changes of corrected responses for the algorithms amount to 8.3 dB (i.e., from  $-22.3 \text{ dB}$  to  $-14.1 \text{ dB}$ ) for (i), 7.8 dB ( $-24.9 \text{ dB}$  to  $-17.1 \text{ dB}$ ) for (ii), 10.9 dB ( $-29.2 \text{ dB}$  to  $-18.3 \text{ dB}$ ) for (iii), 13.1 dB ( $-30.9 \text{ dB}$  to  $-17.8 \text{ dB}$ ) for (iv), and 13.3 dB ( $-30.3 \text{ dB}$  to  $-17 \text{ dB}$ ) for (v). From the results, it is also evident that each method exhibits different performance across the frequency spectrum. Notably, the Morlet-based algorithm (iv) outperforms all of the considered routines in terms of corrected responses fidelity.

Evaluation of the performance metrics for the remaining antennas (provided in Appendix A of the manuscript) supports similar conclusions to the ones drawn for the Vivaldi antenna. For the monopole and quasi-Yagi structures, the performance of (i) is inferior compared to the remaining post-processing routines. Furthermore, the Morlet and MPA routines consistently offer improved correction quality over the remaining algorithms. However, while for quasi-Yagi the performance variation resulting from methods (ii)-(v) is around 1.5 dB (with the lowest average  $e_R$  error of  $-22.8 \text{ dB}$ ), for monopole the change amounts to 7.5 dB (lowest  $e_R$  of  $-28.8 \text{ dB}$ ). Such a significant discrepancy suggests that for compact, low-gain structures, automatic tuning of parameters should be applied along with robust post-processing approach.

Fig. 9 illustrates the MPA correction performance for the Vivaldi and quasi-Yagi antennas expressed in terms of  $e_R$ . For the first structure (cf. Fig. 9(a)), the optimized hyperparameters offer competitive error values in a range from approximately  $-30 \text{ dB}$  to  $-20 \text{ dB}$ , with peak performance at 4 GHz. The other setups are either inferior in terms of performance (with maximum values approaching  $-10 \text{ dB}$ , which is of no use), or

**Table 3**  
Quasi-Yagi – optimized  $B$  and  $K$  for the MPA.

Proposed framework				Setup 1	Setup 2	Setup 3	Setup 4
$f_0$	$K$	$B$	$e_R^S$	$e_R^S$	$e_R^S$	$e_R^S$	$e_R^S$
[GHz]		[GHz]	[dB]	[dB]	[dB]	[dB]	[dB]
4.0	263	3.46	-20.78	-6.27	-5.32	-18.30	-20.45
4.5	259	3.20	-21.22	-6.58	-5.25	-16.77	-21.06
5.0	229	3.50	<b>-23.61</b>	-6.37	-5.56	-18.41	<b>-22.89</b>
5.5	343	3.50	-21.88	-8.36	-5.20	-19.11	-21.85
6.0	343	1.81	-19.74	-8.09	-6.70	-19.85	-19.00
6.5	329	0.84	<b>-24.88</b>	-8.93	-7.11	<b>-23.92</b>	-18.42
7.0	191	0.28	<b>-23.07</b>	-8.28	-7.66	<b>-23.68</b>	-18.19
$\mu_{eR}(R_c(f_0, \theta))$			<b>-22.17</b>	-7.56	-6.11	-20.00	-20.26
$\sigma_{eR}(R_c(f_0, \theta))$			1.78	1.10	1.02	2.76	1.80

<sup>S</sup> $e_R = e_R(R_c(f_0, \theta))$ ; Colormap: green – worst, red – best; Bold font: best average result.

**Table 4**  
Vivaldi – optimized  $B$  and  $K$  vs. correction algorithm.

Alg.	$f_0$ [GHz]	2	3	4	5	6	7	8	9	10	11	12	$\mu_{eR}^\#$
(i)	$K$	59	459	489	489	457	463	437	101	505	599	225	
	$B$ [GHz]	2.95	2.86	0.24	0.24	0.29	0.33	0.37	0.25	2.87	1.33	2.97	
	$e_R^S$ [dB]	<b>-20.52</b>	-14.06	-22.33	-17.71	<b>-19.49</b>	-20.58	-19.69	-19.00	-19.13	-15.74	-18.65	-18.81
(ii)	$K$	165	255	151	59	303	231	147	231	231	183	435	
	$B$ [GHz]	2.75	1.00	2.48	1.12	0.69	3.26	2.50	1.26	1.12	1.35	0.74	
	$e_R^S$ [dB]	-17.67	<b>-23.57</b>	-24.86	<b>-23.45</b>	-17.14	-22.64	-22.45	-24.00	-21.98	-20.78	-19.45	-21.64
(iii)	$K$	61	455	275	95	177	447	355	645	89	109	609	
	$B$ [GHz]	2.95	0.57	3.50	1.80	3.13	3.50	0.46	2.10	0.56	0.31	2.93	
	$e_R^S$ [dB]	-18.87	-20.83	-29.22	-22.62	-18.33	-23.54	<b>-22.73</b>	<b>-24.53</b>	-22.63	-21.05	-18.72	-22.10
(iv)	$K$	51	253	467	651	209	59	79	239	295	533	115	
	$B$ [GHz]	0.84	0.53	0.60	0.87	0.14	0.82	3.37	0.69	0.13	1.67	1.01	
	$e_R^S$ [dB]	-17.79	-23.56	<b>-30.91</b>	-22.29	-19.36	<b>-24.70</b>	-22.37	-23.49	<b>-22.66</b>	-23.88	-20.28	<b>-22.84</b>
(v)	$K$	209	207	209	265	209	261	251	217	371	409	161	
	$B$ [GHz]	1.02	0.54	0.58	0.88	0.17	2.10	1.03	0.78	0.78	1.63	1.06	
	$e_R^S$ [dB]	-17.00	-23.50	-30.30	-22.30	-19.30	-23.90	-22.50	-22.80	-21.80	<b>-24.40</b>	<b>-20.70</b>	-22.60

<sup>#</sup> Denotes average error across frequency band (cf. Table 1).

<sup>S</sup> $e_R = e_R(R_c(f_0, \theta))$ ; Bold font – lowest error.

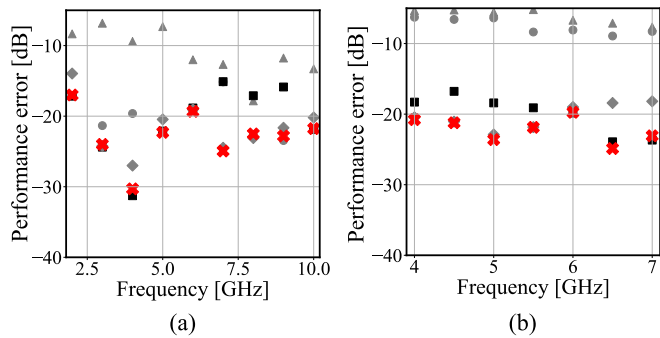


**Fig. 9.** Performance error of the corrected response using the matrix-pencil approach for: (a) Vivaldi antenna and (b) quasi-Yagi antenna. Notation: setup 1 (●), setup 2 (▲), setup 3 (■), setup 4 (◆), and setup 5 (x).

slightly more diverse (frequency-wise). It is worth noting that the range of response changes for the benchmark setups is from -15.2 dB to -23.5 dB for setup 1, from -6.8 dB to -17.8 dB for setup 2, from -15.1 dB to -31.3 dB for setup 3, from -13.9 dB to -27 dB for setup 4, and from -17 dB to -30.3 dB for setup 5, respectively. For the quasi-Yagi structure (see Fig. 9(b)), all of the considered setups represent increased consistency of error values along the frequency spectrum. Nonetheless, the proposed framework offers competitive performance even when compared against the best rule-of-the-thumb setups (i.e., 3 and 4). It should be noted that regardless of competitive performance, one of the greatest advantages of the proposed setup—when compared to state-of-the-art approaches—is the ability to ensure acceptable correction performance without engineering inference.

Fig. 10 shows MPA-based radiation patterns for the spline-based monopole, comparing refined results obtained using automatically tuned hyperparameters with AC-based ones. With a maximum discrepancy of 0.6 dB at 20° at 4.5 GHz and 1.7 dB at 130° at 6 GHz, the resemblance between the responses is considered satisfactory (especially given the rudimentary measurement conditions). Similarly, Figs. 11 and 12 illustrate the responses obtained for the Vivaldi and quasi-Yagi antennas. Again, the refined non-anechoic responses represent substantial improvement w.r.t. AC characteristics, especially when compared with uncorrected data.

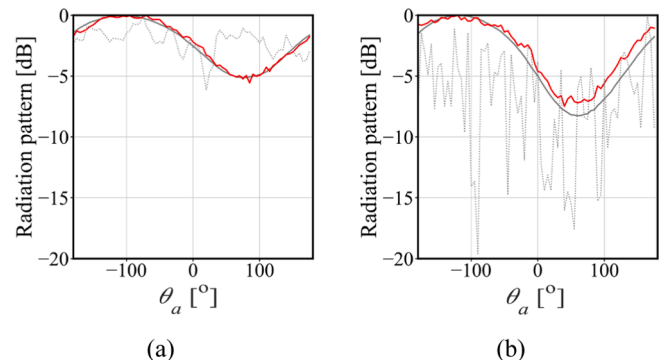


**Fig. 10.** Radiation pattern (normalized gain) comparison for the spline-based monopole antenna far-field responses in xz-plane (cf. Fig. 7) corrected using MPA. Patterns are shown for measurements in an anechoic chamber (gray) and test site A before (●●●), as well as after (red) post-processing at: (a) 4.5 GHz, and (b) 6 GHz.

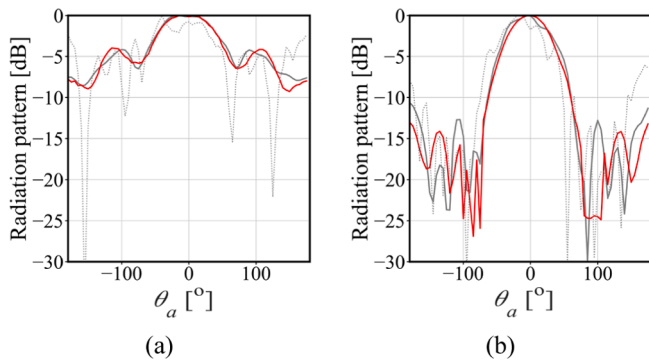


**Fig. 11.** Radiation pattern comparison (normalized gain) for the Vivaldi antenna far-field responses in  $yz$ -plane (cf. Fig. 7) corrected using MPA. Patterns are shown for measurements in an anechoic chamber (gray) and site A before (●●●), as well as after (red) post-processing at: (a) 4 GHz, and (b) 8 GHz.

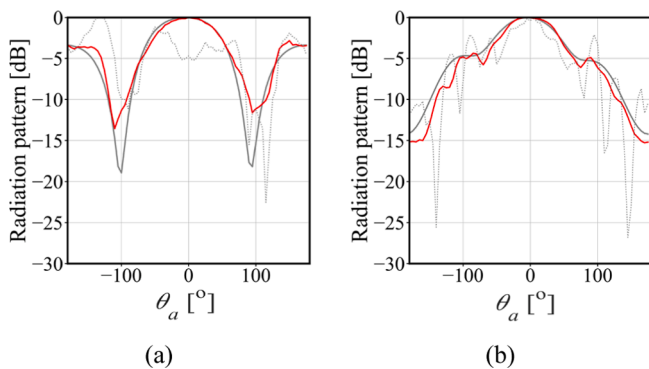


**Fig. 12.** Radiation pattern comparison (normalized gain) for the quasi-Yagi antenna far-field responses in  $yz$ -plane (cf. Fig. 7) using MPA. Patterns are shown for measurements in an anechoic chamber (gray) and at non-anechoic test site A before (●●●) and after (red) post-processing at: (a) 4.5 GHz, and (b) 6.5 GHz.

#### 4.2. Test site B

For the site of Fig. 8(b), the test antennas have been evaluated at the same frequency points and using the same post-processing algorithms as considered in Section 4.1. As it comes to determination of parameters, the first and third setups remained consistent with those used for test site A. Owing to a different time delay in site B, the hyperparameters established for the second setup have been set to  $B = 1.22$  GHz and  $K = 243$  for TGM and Morlet methods, as well as  $B = 0.12$  GHz and  $K = 25$  for MPA. The fourth setup comprised 15 distinct hyperparameter sets (3 antennas  $\times$  5 methods), derived from the functional landscapes of the  $e_R$  errors (cf. Section 4.1). Finally, 125 combinations of  $B$  and  $K$  parameters have been determined based on the guidelines from Section 2.3.

The correction results obtained for the Vivaldi antenna using method (iii) indicate—similarly as in Section 4.1—that the average correction performance is  $-23.1$  dB for the optimized parameters  $K$  and  $B$  (for summary of the results, see Appendix B). For the benchmark setups the post-processing errors range from  $-19.6$  dB to  $-22.5$  dB. It is worth noting that  $\{K, B\}$  of  $\{201, 1$  GHz $\}$  and  $\{81, 1.9$  GHz $\}$  have been determined for setups 1 and 4 based on rule-of-thumb strategies. In addition, the correction results obtained using the proposed framework also exhibit the lowest standard deviation among all setups, at 2.09 dB (with a range from 2.1 dB to 2.6 dB for setups 1–4).

The TGM-based method (iii) has also been used for correction of monopole and quasi-Yagi antenna responses. The setups 1 and 4 for monopole are set to  $\{201, 3$  GHz $\}$  and  $\{51, 3.3$  GHz $\}$ , achieving an average error of  $-20.5$  dB for the automated tuning compared to a range

from  $-13.8$  dB to  $-17.4$  dB for benchmark setups. It is also worth noting that the frequency responses obtained using the automatically determined parameters are characterized by a standard deviation of 2.3 dB, which is the lowest among the compared setups. For the quasi-Yagi structure, setups 1 and 4 are set to  $\{201, 2$  GHz $\}$  and  $\{111, 1.5$  GHz $\}$ , respectively. Again, the automatic adjustment of hyperparameters delivers the average error of  $-23.2$  dB, which is the lowest when compared to benchmark setups (with errors ranging from  $-20.1$  dB to  $-22.4$  dB). Additionally, the automatic setup exhibits the lowest standard deviation of 3.2 dB. For summary of the obtained data, see Appendix B.

Evaluation of the proposed framework for post-processing of non-anechoic measurements performed in site B using algorithms of Section 3 indicates that—for the antennas of Fig. 7—the average correction error (w.r.t. AC measurements) is below  $-20$  dB for all algorithms but (i). It is worth noting that for Vivaldi structure, the best results (average error of  $-23.1$  dB) have been obtained upon coupling the proposed parameter identification framework with method (iii). For monopole and quasi-Yagi radiators, the highest quality of corrected responses of  $-27.3$  dB and  $-24.6$  dB have been obtained using algorithms (v) and (iv), respectively. The data also indicate that different sets of hyperparameters are obtained for each antenna, algorithm, and frequency. It is worth noting that MPA and Morlet-based correction seem to outperform other algorithms for the last two antennas, whereas for Vivaldi, the method (iii) offers slightly (up to  $-0.6$  dB) better performance when compared to algorithms (iv) and (v), respectively. Summary of the performance characteristics can be found in Appendix B.

Fig. 13 illustrates the average correction performance (expressed in terms of  $e_R$ ) obtained using method (iii) for Vivaldi and quasi-Yagi antennas. The average errors vary from  $-16.5$  dB to  $-27$  dB and  $-7$  dB to  $-27$  dB depending on the setup of the Vivaldi and quasi-Yagi structures. Note that for Vivaldi antenna the correction performance obtained using the proposed framework is similar or slightly better compared to most of the setups except for setup 4, which generates responses with noticeably worsened fidelity (cf. Fig. 13(a)). Similarly, for the quasi-Yagi antenna the responses corrected using automatic tuning are similar or slightly better for all considered frequencies except at 6 GHz, where the framework-based response is around  $-2$  dB to  $-0.5$  dB worse compared to benchmark setups (cf. Fig. 13(b)). Fig. 14 presents comparison of the radiation patterns obtained for the monopole antenna at 4.5 GHz and 6 GHz frequencies in AC against the measurements performed in site B before and after correction using algorithm (iii). It should be emphasized that maximum discrepancies (angle-wise) between AC-based and refined measurements amount to 1.2 dB and 1.6 dB for the first and second considered frequency, respectively. Likewise, Figs. 15 and 16 present the adjusted responses for the respective Vivaldi and quasi-Yagi antennas, which show considerable improvements over the uncorrected data.

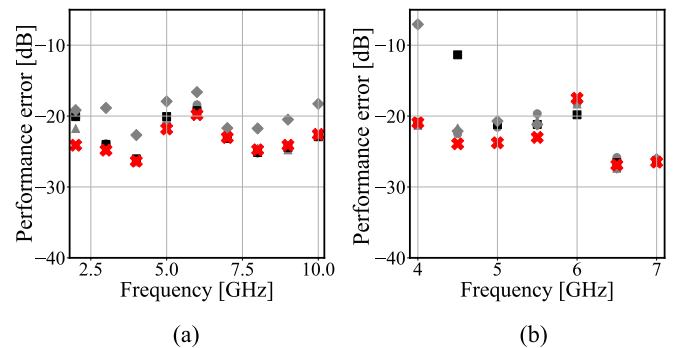


**Fig. 13.** Performance error of the corrected response using the TGM-composite approach for: (a) Vivaldi antenna and (b) quasi-Yagi antenna. Notation: setup 1 (●), setup 2 (▲), setup 3 (■), setup 4 (◆), and setup 5 (x).

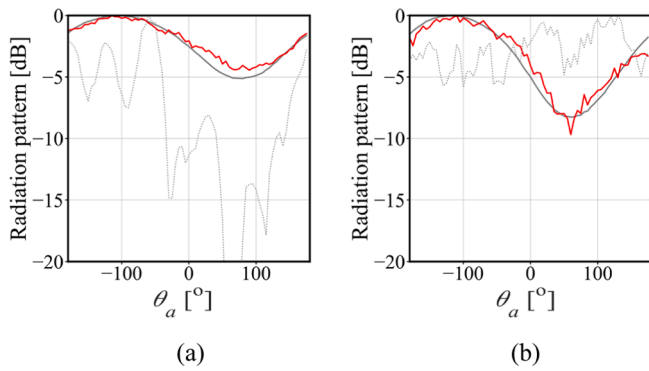


**Fig. 14.** Radiation pattern comparison (normalized gain) for the spline-based monopole far-field responses in  $yz$ -plane (cf. Fig. 7) using TGM-composite. Patterns are shown for measurements in an anechoic chamber (gray) and at non-anechoic test site B before (●●●) and after (red) post-processing at: (a) 4.5 GHz, and (b) 6 GHz.

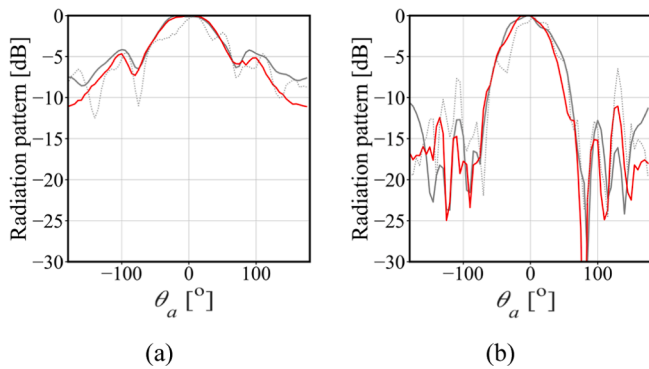


**Fig. 15.** Radiation pattern comparison (normalized gain) for the Vivaldi antenna far-field responses in  $yz$ -plane (cf. Fig. 7) using TGM-composite. Patterns are shown for measurements in an anechoic chamber (gray) and at non-anechoic test site B before (●●●) and after (red) post-processing at: (a) 4 GHz, and (b) 8 GHz.

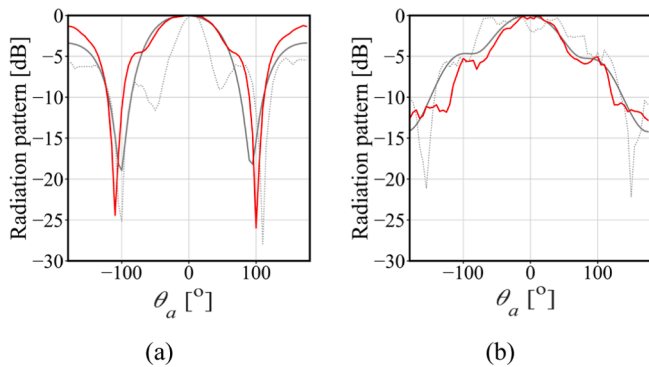


**Fig. 16.** Radiation pattern comparison (normalized gain) for the quasi-Yagi antenna far-field responses in  $yz$ -plane (cf. Fig. 7) using TGM-composite. Patterns are shown for measurements in an anechoic chamber (gray) and at non-anechoic test site B before (●●●) and after (red) post-processing at: (a) 4.5 GHz, and (b) 6.5 GHz.

## 5. Discussion

The proposed framework, systematically compared against conventional post-processing techniques, enables unsupervised optimization-based tuning of correction-specific parameters. As already indicated, the state-of-the-art methods frequently incorporate rule-of-thumb

strategies to set up hyperparameters. These include: (i) determination of a minimum bandwidth  $B$  based on antenna size with a fixed frequency point count  $K$  [38]; (ii) estimation of  $B$  and  $K$  to facilitate effective echo cancellation [9]; (iii) selection of fixed  $B$  and  $K$  values according to typical measurement scenarios; and (iv) adjustment of  $B$  and  $K$  based on thorough evaluation of the error landscape  $e_R$  obtained at the specific antenna and frequency of interest (see Section 2.3). All of the considered benchmark methods generally require some level of expert knowledge to set suitable parameters, which implicitly indicates that determination of correction setup is both time-consuming and error-prone. In contrast, the proposed approach does not rely on engineering expertise (other than the one needed to successfully conduct antenna measurement in AC), or cognitive trial-and-error adjustments. The following sub-sections provide a comprehensive discussion on the capabilities of the proposed framework in terms of ensuring high correction performance. The topics of interest include evaluation of correction errors as a function of setup, antenna type, and post-processing algorithm, alongside the impact of automatic calibration on performance of specific correction algorithms, analysis of post-processing discrepancies obtained in different test-sites, but also evaluation of robustness using analysis of variance (ANOVA). Practical limitations of the framework are also identified and discussed.

### 5.1. Correction error as function of post-processing algorithm and selected setup

The first aspect of interest includes evaluation of the correction quality of the radiation patterns obtained in non-anechoic measurements as a function of selected algorithm and its associated setup. In order to make the results more approachable, the data is averaged across all frequencies of interest considered for the given antennas. The results shown in Tables 5 and 6 gather the  $e_R$  errors obtained within the test sites A and B using all of the correction methods and setups. It should be noted that, for the sake of clarity, the post-processing performance for a setup with automatically determined hyperparameters w.r.t. uncorrected characteristics has been expressed in terms of  $\Delta$  coefficient (in dB).

Despite variations in propagation conditions affected by e.g. site dimensions, furniture arrangement, or external electromagnetic noise—the automatic method offers competitive correction performance that outperforms benchmark setups in most of the considered cases. It is worth noting that for the quasi-Yagi antenna the  $e_R$  error features limited site-to-site variation—i.e., from 0.1 dB for method (i) to 2 dB for method (ii). This contrasts with the rule-of-thumb approaches, which show greater variability, i.e., from 1 dB for method (iv) to 3.9 dB for method (v) when using setup 4, or from 0.1 dB for method (v) to 4 dB for method (ii) when using setup 3 for determination of parameters. For the Vivaldi and monopole antennas, the proposed framework also offers robust performance over the considered frequency range, often achieving the best or highly competitive post-processing errors (regardless of the selected algorithm).

The results obtained in the work suggest that Morlet and MPA methods not only offer relatively high and consistent performance but also tend to outperform TGM-based approaches, especially when coupled with the proposed framework. The main reason is that both methods incorporate rigorous mechanisms for identification of LoS signals. It should be reiterated that, in the case of Morlet-based algorithm, the functionality is enabled through precise evaluation of power responses as a function of RA-AUT angular location. The extracted delays enable precise centering of Gaussian kernel around the useful fraction of the signal in order to suppress noise and interferences (cf. Section 3.2). As it comes to MPA, identification of the signal fraction pertinent to LoS transmission is directly embedded in (14) which enables reconstruction of the refined responses (cf. Section 3.3). In contrast, the algorithms based on TGM are limited to identification of LoS based on rudimentary adjustment of kernels, while not being capable of accounting for their adaptation to changes of RA-AUT angles.

The findings—also supported by the results of Section 4—suggest

Table 5

Test site A – average correction error for all methods.

Alg.	$\mu_{eR}(\mathbf{R}_u)$ [dB]	Setups / $\mu_{eR}(\mathbf{R}_c)$ [dB]					$\Delta^\#$ [dB]	
		1	2	3	4	$P_f^\S$		
Vivaldi	(i)	-15.53	-14.66	-14.90	-14.50	-15.50	-18.81	3.28
	(ii)	-15.53	-21.40	-21.61	-21.42	-20.01	-21.64	5.87
	(iii)	-15.53	-22.06	-21.43	-22.07	-20.44	-22.10	6.57
	(iv)	-15.53	-22.59	-20.77	-22.59	-21.64	-22.84	<b>7.31</b>
	(v)	-15.53	-20.46	-11.90	-20.59	-21.21	-22.60	7.07
Monopole	(i)	-11.97	-10.29	-10.39	-10.49	-10.33	-12.89	0.92
	(ii)	-11.97	-22.46	-22.51	-21.92	-20.46	-23.05	11.08
	(iii)	-11.97	-16.66	-16.21	-16.82	-16.19	-21.26	9.29
	(iv)	-11.97	-28.48	-28.40	-27.59	-27.24	-27.23	15.26
	(v)	-11.97	-8.10	-6.89	-26.10	-28.37	-28.77	<b>16.80</b>
Quasi-Yagi	(i)	-7.77	-14.11	-14.09	-13.31	-17.17	-17.47	9.70
	(ii)	-7.77	-20.03	-19.99	-19.52	-20.56	-21.92	14.15
	(iii)	-7.77	-19.93	-19.94	-19.56	-18.63	-21.32	13.55
	(iv)	-7.77	-19.20	-19.96	-19.61	-20.20	-22.77	<b>15.00</b>
	(v)	-7.77	-7.56	-6.11	-20.00	-20.26	-22.17	14.40

$^\S$ Proposed framework (Colormap: green – worst, red – best).

$^\# \Delta = |\mu_{eR}(\mathbf{R}_u) - \mu_{eR}(\mathbf{R}_c)|$ , with  $\mathbf{R}_c$  obtained for  $P_f$  setup (bold font: best improvement).

Table 6

Test site B – average correction error for all methods.

Alg.	$\mu_{eR}(\mathbf{R}_u)$ [dB]	Setups / $\mu_{eR}(\mathbf{R}_c)$ [dB]					$\Delta^\#$ [dB]	
		1	2	3	4	$P_f^\S$		
Vivaldi	(i)	-14.32	-15.98	-14.11	-15.54	-16.5	-18.27	3.95
	(ii)	-14.32	-21.31	-21.06	-21.15	-20.48	-21.23	6.91
	(iii)	-14.32	-22.36	-22.52	-22.35	-19.64	-23.09	<b>8.77</b>
	(iv)	-14.32	-22.95	-22.65	-22.93	-21.93	-22.78	8.46
	(v)	-14.32	-19.69	-8.57	-22.8	-22.83	-22.48	8.16
Monopole	(i)	-12.14	-10.12	-11.69	-12.03	-11.73	-14.93	2.79
	(ii)	-12.14	-22.15	-23.16	-22.95	-18.92	-22.83	10.69
	(iii)	-12.14	-16.2	-16.74	-17.35	-13.8	-20.47	8.33
	(iv)	-12.14	-25.82	-28.11	-26.67	-25.59	-25.83	13.69
	(v)	-12.14	-10.63	-5.26	-26.07	-25.63	-27.26	<b>15.12</b>
Quasi-Yagi	(i)	-8.07	-11.48	-11.06	-13.83	-15.11	-17.4	9.33
	(ii)	-8.07	-23.17	-23.15	-23.47	-23.65	-23.89	15.82
	(iii)	-8.07	-20.14	-22.39	-21.04	-20.34	-23.21	15.14
	(iv)	-8.07	-21.91	-22.21	-22.45	-21.17	-24.59	<b>16.52</b>
	(v)	-8.07	-7.92	-5.76	-20.09	-16.32	-24.09	16.02

$^\S$ Proposed framework (Colormap: green – worst, red – best).

$^\# \Delta = |\mu_{eR}(\mathbf{R}_u) - \mu_{eR}(\mathbf{R}_c)|$ , with  $\mathbf{R}_c$  obtained for  $P_f$  setup (bold font: best improvement).

that the optimized  $B$  and  $K$  parameters are frequency-dependent. From this perspective, the proposed framework can be used to adjust correction setup w.r.t. the specific antennas and propagation conditions at each frequency. The presented adaptive algorithm remains in contrast to the benchmark methods, which predominantly employ frequency-independent parameters. Notably, the automatic tuning is oriented towards maximization of correction performance by adaptation of setup to environment-specific propagation conditions (both spatial and temporal). It should be noted that, despite varying bandwidths (for the selected frequency and antenna) across considered test sites, the corrected responses remain consistent.

The significance of appropriate algorithm tuning (setup-wise) w.r.t. operational conditions has been demonstrated for the monopole and quasi-Yagi structures, respectively. The experiments performed for the former indicate that, at the 7 GHz frequency, the optimal hyperparameters for site A are  $B = 2.77$  GHz and  $K = 63$ . At the same time values obtained in site B are  $B = 1.12$  GHz and  $K = 495$ . Fig. 17 illustrates comparison of AC measurements of the monopole along with non-anechoic responses obtained in sites A and B corrected using Morlet-based algorithm with setup extracted for site A and B, as well as with swapped setup parameters. Accordingly, Fig. 18 shows comparison of AC-based quasi-Yagi antenna responses at 6.5 GHz against non-AC responses from sites A and B with their optimum setups  $\{B, K\}$  of  $\{0.88$  GHz, 243 $\}$  and  $\{0.78$  GHz, 131 $\}$ , as well as for swapped parameters. The obtained results clearly indicate the significance of appropriate, site-specific setups on the overall correction performance obtained in the

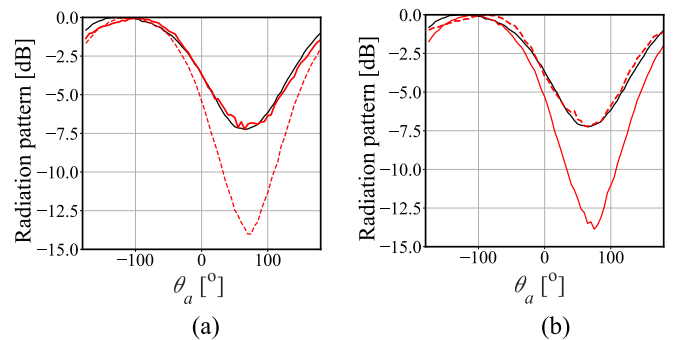
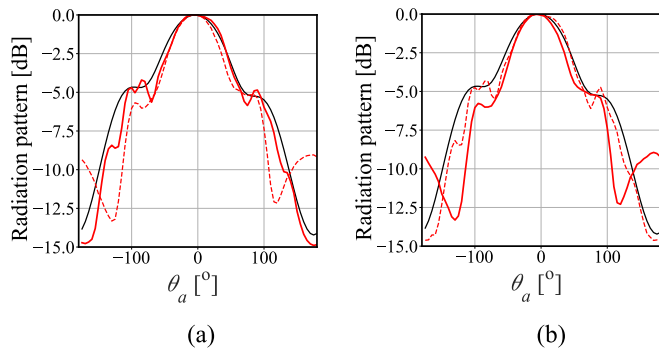


Fig. 17. Morlet-based radiation patterns (normalized gain) of the monopole antenna at 7 GHz (red) compared against AC-based responses (black): (a) non-anechoic responses from site A (optimized  $B = 2.77$  GHz,  $K = 63$ ) corrected using setup based on sites A (—) and B (---), as well as (b) non-anechoic responses from site B (optimized  $B = 1.12$  GHz,  $K = 495$ ) refined for setup based on sites A (—) and B (---), respectively.

considered non-anechoic environments. The alignment of post-processed data (when refined using dedicated setup parameters) with the reference measurements, demonstrates capability of the framework to appropriately adapt performance across varying environmental conditions.



**Fig. 18.** Morlet-based radiation patterns (normalized gain) of the quasi-Yagi antenna at 6.5 GHz (red) compared against AC-based responses (black): (a) non-anechoic responses from site A (optimized  $B = 0.88$  GHz,  $K = 243$ ) corrected using setup based on sites A (—) and B (---), as well as (b) non-anechoic responses from site B (optimized  $B = 0.78$  GHz,  $K = 131$ ) refined for setup based on sites A (—) and B (---), respectively.

### 5.2. Effects of automatic setup on algorithm-specific correction performance

The effects of setup on correction performance are evaluated based on analyses performed in site B for Vivaldi and quasi-Yagi structures using correction methods (iii) and (iv), coupled with the first parameter tuning setup and the proposed automatic framework. Comparisons of the responses obtained for both structures are gathered in [Tables 7 and 8](#), respectively. For the Vivaldi radiator, the results indicate that automatic tuning of the Morlet-based algorithm setup leads to a slight deterioration of correction performance compared to manually configured parameters (the average change ranges from  $-23.2$  dB to  $-22.9$  dB and amounts to  $\sim 0.3$  dB). Simultaneously, for method (iii)—TGM based on composite kernels—an improvement in post-processing performance is noticeable with the optimized setup, amounting to  $\sim 0.7$  dB (from  $-22.7$  dB to  $-23.4$  dB). This represents a slightly greater change in magnitude compared to algorithm (iv). As it comes to the quasi-Yagi structure (cf. [Table 8](#)), the fidelity of corrected responses is noticeably higher when correction is coupled with the proposed parametric optimization framework. The improvements amount to  $\sim 2.7$  dB and  $5.9$  dB, for Morlet- and multi-kernel-based methods, respectively. The gathered data indicate that, although selection of post-processing setup might have noticeable effect on the correction performance, it also depends on the selected algorithm, antenna type, and temporal dynamics of the environment (note that the experiments have been performed within the same test site, yet in a sequence—i.e. they are separated in time). It is worth noting that the deterioration in the average response for Vivaldi due to Morlet-based post-processing can be attributed to its relatively

**Table 7**  
Vivaldi – correction benchmark in site B.

$f_0$ [GHz]	Morlet-based		TGM-composite	
	Setup 1	Optimized	Setup 1	Optimized
2	-17.86	-15.98	-20.09	-24.11
3	-23.58	-22.84	-23.88	-24.81
4	-28.94	-28.12	-26.10	-26.36
5	-21.98	-22.41	-21.02	-21.81
6	-19.28	-19.01	-18.43	-19.79
7	-25.01	-25.11	-23.03	-23.02
8	-25.41	-25.46	-25.23	-24.76
9	-24.49	-24.43	-24.45	-24.13
10	-22.31	-22.63	-22.84	-22.59
11	-22.75	-22.85	-21.83	-22.97
$\mu_{eR}^{\#}$	<b>-23.16</b>	-22.88	-22.69	<b>-23.44</b>

<sup>#</sup> Denotes average error across frequency band (cf. [Table 1](#); bold font: best average result).

**Table 8**  
Quasi-Yagi – correction benchmark in site B.

$f_0$ [GHz]	Morlet-based		TGM-composite	
	Setup 1	Optimized	Setup 1	Optimized
4	-22.80	-23.15	-7.33	-20.27
4.5	-21.84	-22.36	-14.36	-15.81
5	-22.43	-24.42	-7.33	-19.15
5.5	-22.08	-26.96	-10.29	-14.18
6	-21.16	-21.96	-9.44	-13.48
6.5	-22.18	-26.67	-14.75	-18.63
7	-20.91	-26.59	-16.88	-20.23
$\mu_{eR}^{\#}$	-21.91	<b>-24.59</b>	-11.48	<b>-17.40</b>

<sup>#</sup> Denotes average error across frequency band (cf. [Table 1](#); bold font: best average result).

poor performance at the 2 GHz frequency. Since the algorithm maintains tight confinement of the kernel function around the LoS part of the RA-AUT signal (cf. [Section 3.2](#)), its imprecise identification might result in worsened performance. On the other hand, for considered antennas the Morlet-based method demonstrates competitive average performance, regardless of the chosen setup. In the case of multi-kernel algorithm, this is not the case for quasi-Yagi, which can be attributed to lower gain of the antenna, as well as more relaxed definition of kernel which increases the contribution of noise to the overall post-processing performance. From this perspective, combination of robust correction algorithm with routine that enables automatic tuning of its hyperparameters seems justified when the main goal is to maintain acceptable reliability of unsupervised measurements. At the same time, the results highlight the usefulness of hyperparameters tuning for accommodating to antenna type and its frequency-specific characteristics, thereby improving the fidelity of non-anechoic radiation patterns. Apart from evaluation of performance metrics in considered scenarios, the proposed automatic tuning approach indicates the potential for application, across diverse parameter configurations [47]-[48]. Although evaluation of the presented framework in such scenarios is beyond the scope of the manuscript, it might find application for improving error-correction in highly dynamic environments, but also support the development of adaptive algorithms dedicated to optimization of antenna performance in response to environmental variability [47]-[49].

### 5.3. Post-processing performance across the test sites

The measurement environments (test sites) under consideration are distinguished not only by their differing arrangements (cf. [Section 4](#)) but also by temporal dynamics influenced by external sources of EM radiation and their location within the building, which impacts the relative positioning of the measurement setup w.r.t. potential noise sources. From this perspective, variation of the post-processing performance

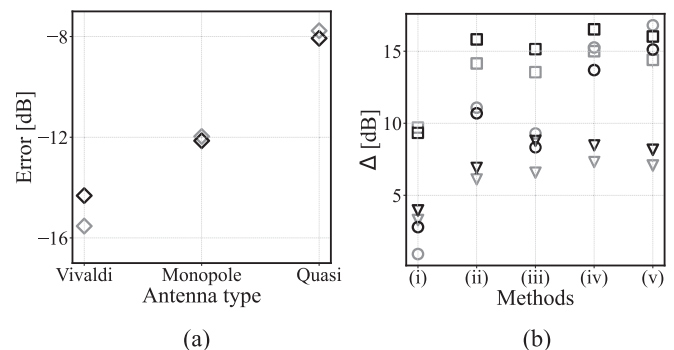


**Fig. 19.** Sites A (gray) and B (black): (a) average  $e_R$  errors for uncorrected responses and (b) uncorrected-to-corrected improvement of performance for considered correction methods and antenna types – Vivaldi ( $\nabla$ ), monopole ( $\circ$ ), and quasi-Yagi ( $\square$ ).

across the sites also represents an interesting point for discussion. Fig. 19 illustrates—averaged for all considered frequencies of interest—discrepancy between the uncorrected response levels from both sites, as well as improvement of refined responses fidelity (expressed as  $\Delta$ ) for the considered correction methods and antennas. The results demonstrate that the averaged  $e_R$  errors for uncorrected responses in site A range from 0.7 dB lower to 1.2 dB higher when compared to site B. It should be noted that for most of the correction algorithms, performance changes between both sites remain comparable. The results indicate that the method (i) is an outlier in terms of performance, which mostly boils down to its rudimentary character (cf. Section 3.1). Furthermore, the methods (iv) and (v) seem to outperform benchmark algorithms regardless of the considered test environment. It is also worth noting that, for the Vivaldi structure, the performance improvement is noticeably lower than for the remaining structures. Given the radiation patterns of Section 4, one could expect that limited improvement of performance (especially compared to other antennas) is due to noticeable discrepancy between AC and refined responses for the angles which correspond to backward orientation of the AUT w.r.t. RA. In such a configuration, the deteriorated signal to noise ratio might reduce the fidelity of extracted radiation response. Further investigation of the problem would require additional measurements in a setup with increased power of the transmitted signal. However, it exceeds the scope of the manuscript. It is worth noting that, owing to reduced front to back ratio, the deterioration of quasi-Yagi performance in backward orientation is less pronounced. At the same time, the problem seems to be relatively limited for a monopole, which features close to omnidirectional characteristics. It should be reiterated that, although environmental conditions affect the signal propagation dynamics and, consequently, the precision of antenna measurements [50–53], the proposed framework (especially, when coupled with robust correction methods) mitigates the negative effects on the fidelity of refined non-anechoic radiation patterns.

Applicability of the proposed framework to improve the fidelity of measurements refined through various correction algorithms highlights its usefulness for complex environments, where automated routine is considered of high importance for mitigating the effects of engineering bias on both the quality and success rate of corrections. Separate tuning for each frequency of interest not only demonstrates adaptability of the presented algorithm to varying propagation conditions but also offers competitive correction performance compared to methods based on rule-of-thumb setups. It should be reiterated that the proposed framework enables consistent minimization of post-processing errors over a broad frequency spectrum and ensures relatively stable performance while not relying on human intervention. Achieving optimal results without manual adjustments makes the method useful for *en-masse* measurements, where labor-intensive manual tuning is not considered as a viable alternative for validation of antenna prototypes.

#### 5.4. Analysis of variance for the proposed framework

The robustness of the proposed framework was evaluated using the one-factor ANOVA in two different scenarios at a significance level of 0.05. In the first case, the test site was chosen as the factor (i.e., independent variable), assessed at two levels (i.e., two groups representing the test-site-specific  $e_R$  errors for each correction method and antenna type). In the second scenario, the correction method was the factor, evaluated at five levels (i.e., five groups representing the correction-specific  $e_R$  errors for each test site and antenna type). The ANOVA results for both considered cases are presented in Table 9 and Table 10, respectively. The presented F-statistic measures the ratio of variance between groups to the variance within groups, while  $p$ -value (derived from the F-statistic) determines the statistical significance. Prior to analysis, the data (i.e.,  $e_R$  errors) for each group was assessed using the Shapiro-Wilk test to confirm a normal distribution [55]. Please note that the size of each group was determined by the number of frequencies of

**Table 9**

The proposed framework: ANOVA over correction methods with test site as a factor.

Alg.	Vivaldi		Monopole		Quasi-Yagi	
	F-statistic	$p$ -value	F-statistic	$p$ -value	F-statistic	$p$ -value
(i)	0.3820	0.5435	1.3845	0.2622	0.0028	0.9588
(ii)	0.1362	0.7160	0.0074	0.9327	2.0740	0.1754
(iii)	0.7564	0.3948	0.3469	0.5668	1.0455	0.3267
(iv)	0.0022	0.9631	0.5220	0.4838	3.4538	0.0878
(v)	0.0081	0.9293	0.4877	0.4983	4.0099	0.0684

**Table 10**

The proposed framework: ANOVA over test sites with correction method as a factor.

Site	Vivaldi		Monopole		Quasi-Yagi	
	F-statistic	$p$ -value	F-statistic	$p$ -value	F-statistic	$p$ -value
A	3.2725	0.0186	26.0938	2.16e-09	4.1032	0.0091
B	6.3071	3.41e-04	9.6192	3.96e-05	10.8274	1.49e-05

interest specific to each antenna structure (11 for Vivaldi and 7 each for monopole and quasi-Yagi).

Based on the results for the first scenario (cf. Table 9), the proposed framework demonstrates robustness to the change of the test site, regardless of the correction method applied. All obtained  $p$ -values are significantly greater than 0.05, leading to the acceptance of the null hypothesis, which indicates no statistically significant difference between the means of the two considered groups for each correction variant and antenna type.

When analyzing the results for the second scenario (cf. Table 10), the obtained  $p$ -values for each test site and antenna structure are significantly lower than the assumed 0.05 significance level, leading to the rejection of the null hypothesis. Subsequently, Tukey's Honest Significant Difference test was conducted to determine the discrepancies between group means [55]. In all cases, the group representing  $e_R$  errors for correction method (i), which utilizes TGM with a rectangular kernel, exhibited a mean significantly different from the averages obtained for the remaining groups, regardless of the test site or antenna structure. This result translates to worsened correction performance (higher  $e_R$  errors) compared to other correction methods, a trend that is also evident across different setups. These findings suggest that the proposed framework maintains robustness to changes in the correction method when considering post-processing approaches other than TGM-based correction.

#### 5.5. Limitations of the method

The proposed framework for automatic tuning of post-processing algorithms offers notable advantages compared to the existing rule-of-thumb-based approaches. Notwithstanding, the method has limitations that stem from the character of the curve-fitting process outlined in Section 2.3 and associated assumptions. First, the application of the framework is subject to existence of either the EM model (i.e., a representation of the antenna prototype under test), or (at least) EM-based radiation responses of the structure. In other words, minimization of (2) cannot be performed if EM-based data (associated with the given AUT at frequencies of interest) is not available for the user. On the other hand, given that the main goal of the presented mechanism is low-cost validation of antenna prototypes, the requirement concerning existence of EM model should be fulfilled in most practical scenarios. However, assuming that only a prototype structure is available, its corresponding EM model must be reconstructed. It is worth noting that, for many structures (especially planar), the process should be relatively straightforward. It could involve measurements of prototype dimensions

followed by manual implementation of the model in the EM simulation software of choice. Alternatively, automatic generation can be performed based on photographs, or schematic diagrams of the prototype structure [56].

Another potential limitation of the method—that stem from the algorithm of Section 2.3—is the implicit assumption of similarity behind EM simulation responses and measurement results. As already demonstrated (e.g., based on the results obtained for the monopole antenna), the aforementioned similarity can be perceived in a relatively broad manner. This is mostly because, owing to the use of uniform scaling coefficient, the difference between  $R_c(x)$  and  $R_0$  amplitudes as a function of RA-AUT angles is of lesser concern for curve-fitting. Notwithstanding, discrepancy resulting from incorrect EM model setup, or systematic errors (e.g., frequency shift of resonances resulting from imprecise definition of substrate electrical parameters) might pose a serious limitation in terms of algorithm reliability [54]. Despite its significance, the problem can be mitigated based on evaluation of discrepancies between EM-based and measured reflection characteristics of the AUT. In most practical cases, reflection responses—which, incidentally, are much easier to obtain compared to far-field data—can serve as indicators of resemblance between the prototype and the EM model, and hence correctness of the latter. Furthermore, in the case of unacceptable discrepancies, the model can be adjusted so as to improve its fidelity w.r.t. measurements. In essence, the task can be reformulated as an optimization process oriented towards prototype-augmented refinement of EM simulation responses. Clearly, such a concept exceeds the scope of this work and thus will not be discussed in more details.

It is worth noting that measurement uncertainties associated to noise, temporal dynamics of the search space, but also factors such as RA-AUT alignment, repeatability of interconnections, or calibration of the test equipment might pose challenges in maintaining consistent correction performance. Although the problem exceeds the scope of this work, further discussion on the related issues and their effects on fidelity of post-processed measurements can be found in [11,20,51,57].

In summary, regardless of reliance on the availability of EM simulations for correction, the absence of an appropriate model or its poor fidelity does not prohibit automatic tuning. In this regard, improvement of model quality (or its development) represents a preliminary step before its application to correction for non-anechoic measurements. It should be emphasized that, owing to advancements in computational electromagnetics over the past few decades (and availability of advanced simulation packages), development, discretization and evaluation of EM models—while not error-free—became relatively simple and streamlined. From this perspective, the lack of EM simulation or their insufficient fidelity does not pose a substantial challenge for the use of the proposed framework.

## Appendix

The appendix contains supplementary tables with data obtained in test sites A and B for the considered correction algorithms and setups. The results refer to the discussion provided in Section 4 of the manuscript.

### A. Test site A

Tables A1 and A2 gather data on performance of the considered post-processing algorithms coupled with the proposed framework for automatic adjustment of hyperparameters. The discussion related to the Tables A1 and A2 is contained in Section 4.1.

## 6. Conclusions

A framework for automatic determination of post-processing parameters for antenna measurements performed in non-anechoic environments has been proposed. The method mitigates the limitations inherent to traditional, rule-of-thumb-based methods for correction setup. Application of rigorous numerical optimization enables precise selection of both bandwidth and frequency resolution for a variety of post-processing routines. The framework has been extensively validated through a large body of experiments conducted at two different test sites, incorporating three antennas types, five post-processing techniques and five methods for set-up of hyperparameters. The results quantitatively demonstrate capability of unsupervised tuning to improve fidelity of measurements performed in uncontrolled environments compared to conventional, cognition-driven methods. It was also observed that the optimal bandwidth and frequency resolution are contingent not only on the antenna type but also on its operating frequency and the propagation conditions present within the measurement environment.

Future work will focus on development of self-calibration mechanisms that obviate the need for comparison against EM simulation responses for improvement of post-processing performance. Development of methods dedicated to adaptive correction of measurements performed in highly dynamic (in terms of temporal changes) non-anechoic environments will also be considered.

### CRedit authorship contribution statement

**Adrian Bekasiewicz:** Writing – review & editing, Writing – original draft, Visualization, Supervision, Software, Resources, Project administration, Methodology, Funding acquisition, Conceptualization. **Mariusz Dzwonkowski:** Writing – review & editing, Writing – original draft, Validation, Software, Methodology, Investigation, Formal analysis, Data curation. **Vorya Waladi:** Writing – review & editing, Writing – original draft, Visualization, Validation, Software, Methodology, Investigation, Formal analysis, Data curation.

### Declaration of competing interest

The authors declare that they have no known competing financial interests or personal relationships that could have appeared to influence the work reported in this paper.

### Acknowledgements

This work was supported in part by the National Science Center of Poland Grant 2021/43/B/ST7/01856.

**Table A1**  
Monopole – optimized  $B$  and  $K$  vs. correction algorithm.

Alg.	$f_0$ [GHz]	3.5	4.0	4.5	5.0	5.5	6.0	6.5	$\mu_{eR}$ #
(i)	$K$	371	507	499	371	51	231	197	-12.89
	$B$ [GHz]	0.21	1.21	1.03	0.21	1.03	3.26	0.29	
	$e_R^S$ [dB]	-10.08	-12.30	-10.47	-16.58	-12.02	-12.23	-16.57	
(ii)	$K$	479	73	147	51	51	441	51	-23.05
	$B$ [GHz]	0.78	1.90	2.38	1.88	2.15	1.50	2.27	
	$e_R^S$ [dB]	-18.80	-27.08	-20.14	-21.34	-24.51	-18.02	<b>-31.46</b>	
(iii)	$K$	475	59	71	505	209	567	569	-21.26
	$B$ [GHz]	3.27	2.93	2.44	1.67	0.99	0.33	0.27	
	$e_R^S$ [dB]	-17.39	-19.54	-22.83	-24.07	-24.48	-19.39	-21.11	
(iv)	$K$	271	207	493	271	231	129	51	-27.23
	$B$ [GHz]	1.35	3.30	3.36	3.50	2.79	3.50	1.13	
	$e_R^S$ [dB]	-29.37	-31.18	-28.47	-23.82	-23.50	-26.41	-27.88	
(v)	$K$	307	311	259	279	239	425	355	<b>-28.77</b>
	$B$ [GHz]	3.16	1.32	3.19	3.31	3.47	2.10	2.91	
	$e_R^S$ [dB]	<b>-30.40</b>	<b>-31.68</b>	<b>-29.20</b>	<b>-24.57</b>	<b>-26.31</b>	<b>-29.84</b>	-29.39	

# Denotes average error across frequency band (cf. Table 1).

S  $e_R = e_R(\mathbf{R}_c(f_0, \theta))$ ; Bold font – lowest error.

**Table A2**  
Quasi-Yagi – optimized  $B$  and  $K$  vs. correction algorithm.

Alg.	$f_0$ [GHz]	4.0	4.5	5.0	5.5	6.0	6.5	7.0	$\mu_{eR}$ #
(i)	$K$	51	145	483	243	453	297	251	-17.47
	$B$ [GHz]	1.36	1.03	0.89	0.31	0.24	1.36	1.93	
	$e_R^S$ [dB]	-20.93	-15.20	-13.54	-16.02	-17.02	-20.72	-18.88	
(ii)	$K$	137	115	235	109	111	55	51	-21.92
	$B$ [GHz]	0.61	2.04	0.83	2.82	2.38	3.05	1.76	
	$e_R^S$ [dB]	-22.05	-21.81	-16.87	-19.13	<b>-21.48</b>	-26.33	<b>-25.75</b>	
(iii)	$K$	233	67	439	109	145	71	115	-21.32
	$B$ [GHz]	1.15	2.10	3.44	2.82	3.13	2.97	0.67	
	$e_R^S$ [dB]	-20.13	-17.15	-22.66	-19.13	-18.77	<b>-27.13</b>	-24.84	
(iv)	$K$	51	67	83	99	343	243	93	<b>-22.77</b>
	$B$ [GHz]	2.70	3.44	3.46	3.50	1.66	0.88	0.23	
	$e_R^S$ [dB]	<b>-22.30</b>	<b>-22.37</b>	-23.10	<b>-22.65</b>	-20.33	-24.71	-24.02	
(v)	$K$	263	259	229	343	343	329	191	-22.17
	$B$ [GHz]	3.46	3.20	3.50	3.50	1.81	0.84	0.28	
	$e_R^S$ [dB]	-20.78	-21.22	<b>-23.61</b>	-21.88	-19.74	-24.88	-23.07	

# Denotes average error across frequency band (cf. Table 1).

S  $e_R = e_R(\mathbf{R}_c(f_0, \theta))$ ; Bold font – lowest error. B. Test site B

Tables B1-B3 summarize the performance of multi-kernel correction method (iii) for rule-of-thumb-based and automatic parameter adjustment setups. Tables B4-B6 gather data on performance of the considered post-processing algorithms coupled with the proposed framework. The discussion related to the Tables B1-B6 is contained in Section 4.2 of the paper.

**Table B1**  
Vivaldi – optimized  $B$  and  $K$  for the method (iii).

Proposed framework				Setup 1	Setup 2	Setup 3	Setup 4
$f_0$ [GHz]	$K$	$B$ [GHz]	$e_R^S$ [dB]	$e_R^S$ [dB]	$e_R^S$ [dB]	$e_R^S$ [dB]	$e_R^S$ [dB]
2	371	3.41	-24.11	-20.09	-21.76	-20.08	-19.16
3	273	3.50	-24.81	-23.88	-24.79	-24.01	-18.85
4	651	2.93	<b>-26.36</b>	-26.1	-26.47	-26.03	-22.68
5	199	0.78	-21.81	-21.02	-20.01	-20.07	-17.93
6	281	2.14	-19.79	-18.43	-18.36	-19.23	-16.62
7	351	3.49	-23.02	-23.03	-23.17	-23.15	-21.69
8	87	1.31	-24.76	-25.23	-24.55	-25.13	-21.75
9	111	2.35	-24.13	-24.45	-24.78	-24.45	-20.5
10	249	3.50	-22.59	-22.84	-22.9	-22.91	-18.27
11	87	3.44	-22.97	-21.83	-21.76	-21.72	-21.64
12	431	3.24	-19.59	-19.04	-19.18	-19.02	-16.97
$\mu_{eR}(\mathbf{R}_c(f_0, \theta))$			<b>-23.09</b>	-22.36	-22.52	-22.35	-19.64
$\sigma_{eR}(\mathbf{R}_c(f_0, \theta))$			2.09	2.52	2.58	2.47	2.11

S  $e_R = e_R(\mathbf{R}_c(f_0, \theta))$ ; Colormap: green – worst, red – best; Bold font: best average result.

**Table B2**  
Monopole – optimized  $B$  and  $K$  for the method (iii).

Proposed framework				Setup 1	Setup 2	Setup 3	Setup 4
$f_0$ [GHz]	$K$	$B$ [GHz]	$e_R^S$ [dB]	$e_R^S$ [dB]	$e_R^S$ [dB]	$e_R^S$ [dB]	$e_R^S$ [dB]
3.5	205	2.00	<b>-20.13</b>	-11.22	-9.30	-9.43	-9.58
4.0	541	0.60	-16.47	-13.13	-13.71	-14.55	-10.65
4.5	439	2.90	-19.19	-15.55	-16.07	-15.65	-16.37
5.0	591	3.20	-20.01	-15.53	-17.98	-17.89	-15.04
5.5	349	3.26	-21.67	-18.42	-18.97	-21.19	-14.86
6.0	163	0.33	-22.32	-18.12	-20.85	-19.93	-14.35
6.5	177	0.67	-23.53	-21.43	-20.33	-22.82	-15.75
$\mu_{eR}(\mathbf{R}_c(f_0, \theta))$			<b>-20.47</b>	-16.20	-16.74	-17.35	-13.80
$\sigma_{eR}(\mathbf{R}_c(f_0, \theta))$			2.32	3.44	4.11	4.57	2.62

<sup>S</sup>  $e_R = e_R(\mathbf{R}_c(f_0, \theta))$ ; Colormap: green – worst, red – best; Bold font: best average result.

**Table B3**  
Quasi-Yagi – optimized  $B$  and  $K$  for the method (iii).

Proposed framework				Setup 1	Setup 2	Setup 3	Setup 4
$f_0$ [GHz]	$K$	$B$ [GHz]	$e_R^S$ [dB]	$e_R^S$ [dB]	$e_R^S$ [dB]	$e_R^S$ [dB]	$e_R^S$ [dB]
4.0	0.35	1.78	-20.93	<b>-7.08</b>	-21.31	-20.89	<b>-7.06</b>
4.5	2.93	2.47	-23.91	-22.49	-21.69	-11.36	-22.12
5.0	0.53	2.48	-23.77	-21.57	-20.83	-21.21	-20.71
5.5	3.27	3.23	-23.01	-19.67	-20.68	-21.18	-21.18
6.0	3.27	1.80	-17.49	-18.19	-18.30	-19.82	-17.99
6.5	3.50	0.54	-26.90	-25.85	-27.36	-26.57	-27.27
7.0	0.21	0.53	-26.49	-26.15	-26.56	-26.27	-26.07
$\mu_{eR}(\mathbf{R}_c(f_0, \theta))$			<b>-23.21</b>	-20.14	-22.39	-21.04	-20.34
$\sigma_{eR}(\mathbf{R}_c(f_0, \theta))$			3.24	6.47	3.31	5.05	6.67

<sup>S</sup>  $e_R = e_R(\mathbf{R}_c(f_0, \theta))$ ; Colormap: green – worst, red – best; Bold font: best average result.

**Table B4**  
Vivaldi – optimized  $B$  and  $K$  vs. correction algorithm.

Alg.	$f_0$ [GHz]	2	3	4	5	6	7	8	9	10	11	12	$\mu_{eR}^{\#}$
(i)	$K$	53	105	413	501	235	213	459	511	489	491	493	
	$B$ [GHz]	2.59	3.39	0.55	0.10	0.11	0.10	0.83	0.14	0.31	0.33	0.33	
	$e_R^S$ [dB]	-19.41	-17.51	-18.15	-15.22	-15.69	-19.48	-21.33	-18.30	-18.50	-18.95	-18.48	-18.27
(ii)	$K$	91	459	489	223	315	511	399	59	219	247	253	
	$B$ [GHz]	2.68	0.95	0.99	1.02	0.92	0.85	0.99	2.49	0.99	0.78	0.92	
	$e_R^S$ [dB]	-18.00	-22.30	-24.03	-17.88	-17.14	-22.75	-23.76	-23.38	<b>-22.89</b>	-21.68	-19.73	-21.23
(iii)	$K$	371	273	651	199	281	351	87	111	249	87	431	
	$B$ [GHz]	3.41	3.50	2.93	0.78	2.14	3.49	1.31	2.35	3.50	3.44	3.24	
	$e_R^S$ [dB]	<b>-24.11</b>	<b>-24.81</b>	-26.36	-21.81	<b>-19.79</b>	-23.02	-24.76	-24.13	-22.59	<b>-22.97</b>	-19.59	<b>-23.09</b>
(iv)	$K$	59	357	271	413	239	495	253	145	507	51	51	
	$B$ [GHz]	1.28	0.50	0.44	0.82	0.48	1.12	0.10	1.08	0.12	0.89	1.12	
	$e_R^S$ [dB]	-15.98	-22.84	-28.12	<b>-22.41</b>	-19.01	<b>-25.11</b>	<b>-25.46</b>	<b>-24.43</b>	-22.63	-22.85	<b>-21.72</b>	-22.78
(v)	$K$	397	331	347	331	269	247	433	205	127	273	147	
	$B$ [GHz]	0.98	0.78	0.78	0.80	0.48	1.80	0.10	0.15	0.44	0.95	1.80	
	$e_R^S$ [dB]	-17.64	-22.64	<b>-29.22</b>	-22.31	-18.72	-24.84	-23.75	-22.63	-22.32	-22.72	-20.45	-22.48

<sup>#</sup> Denotes average error across frequency band (cf. Table 1).

<sup>S</sup>  $e_R = e_R(\mathbf{R}_c(f_0, \theta))$ ; Bold font – lowest error.

**Table B5**  
Monopole – optimized  $B$  and  $K$  vs. correction algorithm.

Alg.	$f_0$ [GHz]	3.5	4.0	4.5	5.0	5.5	6.0	6.5	$\mu_{eR}^{\#}$
(i)	$K$	419	111	463	443	283	511	63	
	$B$ [GHz]	0.10	1.23	0.99	0.16	0.11	0.10	0.60	
	$e_R^S$ [dB]	-8.34	-14.15	-14.35	-14.66	-14.83	-20.52	-17.65	-14.93
(ii)	$K$	169	651	431	503	581	651	365	
	$B$ [GHz]	0.67	2.51	1.46	1.33	1.80	1.80	0.85	
	$e_R^S$ [dB]	-15.35	-27.48	-29.00	-22.42	-24.78	-21.21	-19.57	-22.83
(iii)	$K$	205	541	439	591	349	163	177	
	$B$ [GHz]	2.00	0.60	2.90	3.20	3.26	0.33	0.67	
	$e_R^S$ [dB]	-20.13	-16.47	-19.19	-20.01	-21.67	-22.32	<b>-23.53</b>	-20.47
(iv)	$K$	451	645	615	631	431	299	339	
	$B$ [GHz]	2.71	2.45	2.48	3.50	2.78	0.72	3.50	
	$e_R^S$ [dB]	<b>-29.26</b>	<b>-31.74</b>	-28.92	-24.56	-24.57	-21.83	-19.95	-25.83
(v)	$K$	363	441	411	279	291	317	389	

(continued on next page)

Table B5 (continued)

Alg.	$f_0$ [GHz]	3.5	4.0	4.5	5.0	5.5	6.0	6.5	$\mu_{eR}$ #
	$B$ [GHz]	2.54	2.47	3.50	3.50	2.48	1.80	3.46	
	$e_R^S$ [dB]	-26.84	-27.76	<b>-37.67</b>	<b>-27.21</b>	<b>-25.76</b>	<b>-24.92</b>	-20.65	<b>-27.26</b>

# Denotes average error across frequency band (cf. Table 1).

 $e_R^S = e_R(\mathbf{R}_c(f_0, \theta))$ ; Bold font – lowest error.

Table B6

Quasi-Yagi – optimized  $B$  and  $K$  vs. correction algorithm.

Alg.	$f_0$ [GHz]	4.0	4.5	5.0	5.5	6.0	6.5	7.0	$\mu_{eR}$ #
(i)	$K$	415	567	561	387	271	421	511	
	$B$ [GHz]	0.23	2.35	0.19	0.40	0.35	0.16	0.40	
	$e_R^S$ [dB]	-20.27	-15.81	-19.15	-14.18	-13.48	-18.63	-20.23	-17.40
(ii)	$K$	251	165	111	287	351	105	289	
	$B$ [GHz]	1.74	2.54	2.38	0.82	2.47	3.13	0.91	
	$e_R^S$ [dB]	-21.41	<b>-23.95</b>	<b>-25.07</b>	-23.10	<b>-23.51</b>	-25.28	-24.92	-23.89
(iii)	$K$	511	271	347	651	331	231	169	
	$B$ [GHz]	0.35	2.93	0.53	3.27	3.27	3.50	0.21	
	$e_R^S$ [dB]	-20.93	-23.91	-23.77	-23.01	-17.49	<b>-26.90</b>	-26.49	-23.21
(iv)	$K$	281	361	51	51	379	131	77	
	$B$ [GHz]	1.95	2.28	3.08	3.14	2.29	0.78	0.14	
	$e_R^S$ [dB]	<b>-23.15</b>	-22.36	-24.42	<b>-26.96</b>	-21.96	-26.67	<b>-26.59</b>	<b>-24.59</b>
(v)	$K$	245	79	345	201	451	403	331	
	$B$ [GHz]	1.78	2.47	2.48	3.23	1.80	0.54	0.53	
	$e_R^S$ [dB]	-23.05	-23.01	-23.63	-24.90	-21.47	-26.49	-26.10	-24.09

# Denotes average error across frequency band (cf. Table 1).

 $e_R^S = e_R(\mathbf{R}_c(f_0, \theta))$ ; Bold font – lowest error.

## Data availability

Data will be made available on request.

## References

- [1] G. Kim, S. Kim, Design and analysis of dual polarized broadband microstrip patch antenna for 5G mmWave antenna module on FR4 substrate, *IEEE Access* 9 (2021) 64306–64316.
- [2] J.-W. Kim, J.-I. Oh, S.H. Han, W.-Y. Song, S.-C. Chae, J.-W. Yu, Wideband circularly polarized antenna with reconfigurable 2-dimensional axial ratio beamwidth, *IEEE Access* 9 (2021) 79927–79935.
- [3] A. Yaghjian, An overview of near-field antenna measurements, *IEEE Trans. Ant. Prop.* 34 (1) (1986) 30–45.
- [4] S. Gregson, J. McCormick, C. Parini, Principles of planar near-field antenna measurements, The Institution of Engineering and Technology, IET Electromagnetic waves series 53 (2007).
- [5] V. Kalashnikov, et al., Near Field Antenna Measurements: Calculations and Facility Design, Springer, 2021.
- [6] A. Bekasiewicz, S. Koziel, Structure and design optimisation of compact UWB slot antenna, *Electronics Lett.* 52 (9) (2016) 681–682.
- [7] J.D. Krieger, E.H. Newman, L.J. Gupta, The single antenna method for the measurement of antenna gain and phase, *IEEE Trans. Ant. Prop.* 54 (11) (2006) 3562–3565.
- [8] L. Hemming, Electromagnetic Anechoic Chambers: A fundamental Design and Specification Guide, IEEE Press, Piscataway, 2002.
- [9] S. Loredo, M.R. Pino, F. Las-Heras, T.K. Sarkar, Echo identification and cancellation techniques for antenna measurement in non-anechoic test sites, *IEEE Ant. Prop. Mag.* 46 (1) (2004) 100–107.
- [10] A. Soltane, G. Andrieu, E. Perrin, C. Decroze, A. Reineix, Antenna radiation pattern measurement in a reverberating enclosure using the time-gating technique, *IEEE Ant. Wireless Prop. Lett.* 19 (1) (2020) 183–187.
- [11] S. Kurokawa, M. Hirose, K. Komiyama, Measurement and uncertainty analysis of free-space antenna factors of a log-periodic antenna using time-domain techniques, *IEEE Trans. Instrumentation Meas.* 58 (4) (2009) 1120–1125.
- [12] A.N. Sao Jose, V. Deniau, U.C. Resende, R. Adriano, Improving antenna gain estimations in non-ideal test sites with auto-tunable filters, *Measurement* 159 (2020) 107720, <https://doi.org/10.1016/j.measurement.2020.107720>.
- [13] E.F. Knott, et al., Radar Cross Section, 2nd ed., Artech House, Boston, 1993.
- [14] W.D. Burnside, et al., An enhanced tapered chamber design, *Ant. Meas. Tech. Assoc. Proc.*, Monterey Bay, CA, 1999.
- [15] X. Li, L. Chen, Z. Wang, K. Yang, J. Miao, An ultra-wideband plane wave generator for 5G base station antenna measurement, *Electronics* 12 (2022), art no. 1824.
- [16] F. Zhang, Y. Zhang, Z. Wang, W. Fan, Plane wave generator in non-anechoic radio environment, *IEEE Ant. Wireless Prop. Lett.* 22 (12) (2023) 2896–2900.
- [17] F. Scattone et al., Production measurement of 5G millimeter wave plane wave generators, *European Conf. Ant. Prop.*, Madrid, Spain, 2022, pp. 1–3.
- [18] P. Piasecki, J. Strycharz, Measurement of an omnidirectional antenna pattern in an anechoic chamber and an office room with and without time domain signal processing, *Signal Proc. Symp.*, Debe, Poland, 2015, pp. 1–4.
- [19] V. Molina-Lopez, M. Botello-Perez, I. Garcia-Ruiz, Validation of the open-area antenna calibration site at CENAM, *IEEE Trans. Instrumentation Meas.* 58 (4) (2009) 1126–1134.
- [20] A. Bekasiewicz, S. Koziel, M. Czyz, Time-gating method with automatic calibration for accurate measurements of electrically small antenna radiation patterns in nonanechoic environments, *Measurement* 208 (2023) 112477.
- [21] V. Fiumara, A. Fusco, G. Iadarola, V. Matta, I.M. Pinto, Free-space antenna pattern retrieval in nonideal reverberation chambers, *IEEE Trans. EM Comp.* 58 (3) (2016) 673–677.
- [22] G. Leon, S. Loredo, S. Zapatero, F. Las-Heras, Radiation pattern retrieval in nonanechoic chambers using the matrix pencil algorithm, *Prog. EM. Res. Lett.* 9 (2009) 119–127.
- [23] Z. Du, J.I. Moon, S.-S. Oh, J. Koh, T.K. Sarkar, Generation of free space radiation patterns from non-anechoic measurements using Chebyshev polynomials, *IEEE Trans. Ant. Prop.* 58 (8) (2010) 2785–2790.
- [24] D.A. Leatherwood, E.B. Joy, Plane wave, pattern subtraction, range compensation, *IEEE Trans. Ant. Prop.* 49 (12) (2001) 1843–1851.
- [25] B. Fourestie, Z. Altman, Gabor schemes for analyzing antenna measurements, *IEEE Trans. Ant. Prop.* 49 (9) (2001) 1245–1253.
- [26] B. Fourestie, Z. Altman, J. Wiart, A. Azoulay, On the use of the matrix-pencil method to correlate measurements at different test sites, *IEEE Trans. Ant. Prop.* 47 (10) (1999) 1569–1573.
- [27] E.N. Clouston, P.A. Langsford, S. Evans, Measurement of anechoic chamber reflections by time-domain techniques, *IEE Proc.* 135 (2) (1988) 93–97.
- [28] S. Loredo, G. Leon, S. Zapatero, F. Las-Heras, Measurement of low-gain antennas in non-anechoic test sites through wideband channel characterization and echo cancellation, *IEEE Ant. Prop. Mag.* 51 (1) (2009) 128–135.
- [29] Y. Su, S. Gong, Reflection suppression through modal filtering for wideband antenna measurement in a non-absorbent environment, *Electronics* 11 (20) (2022) 3422.
- [30] F.J. Cano-Facila, S. Burgos, F. Martín, M. Sierra-Castaner, New reflection suppression method in antenna measurement systems based on diagnostic techniques, *IEEE Trans. Ant. Prop.* 59 (3) (2011) 941–949.
- [31] P. Gonzalez-Blanco, M. Sierra-Castaner, Analysis of time filtering techniques for echo reduction in antenna measurements, *Int. J. Microwave Wireless Tech.* 9 (7) (2017) 1387–1395.
- [32] J. Koh, et al., Free space radiation pattern reconstruction from non-anechoic measurements using an impulse response of the environment, *IEEE Trans. Ant. Prop.* 60 (2) (2012) 821–831.
- [33] C.H. Schmidt, T.F. Eibert, Near-field far-field transformation in echoic measurement environments employing scattering center representations, *European Conf. Ant. Prop.*, Berlin, Germany, 2009, pp. 3370–3374.
- [34] J.L. Araque Quijano et al., Source reconstruction in advanced processing of antenna measurements, *European Conf. Ant. Prop.*, Rome, Italy, 2011, pp. 3875–3879.

- [35] Y.A. Lopez, J. Laviada, C. Garcia-Gonzalez, F. Las-Heras, Antenna characterization with multiple scatterers by means of equivalent currents and spherical wave expansion, *European Conf. Ant. Prop.*, Prague, Czech Republic, 2012, pp. 2551–2554.
- [36] S.M. Froes, P. Corral, M.S. Novo, M. Aljaro, A.C.C. Lima, Antenna radiation pattern measurement in a nonanechoic chamber, *IEEE Ant. Wireless Prop. Lett.* 18 (2) (2019) 383–386.
- [37] J. Mroczka, The cognitive process in metrology, *Measurement* 46 (2013) 2896–2907.
- [38] A. Bekasiewicz, V. Waladi, Filter-Hilbert method for automatic correction of non-anechoic antenna measurements with embedded self-calibration mechanism, *Measurement* 222 (2023) 113705, <https://doi.org/10.1016/j.measurement.2023.113705>.
- [39] A. Bekasiewicz, V. Waladi, Automatic correction of non anechoic antenna measurements using complex Morlet wavelets, *IEEE Ant. Wireless Prop. Lett.* 23 (8) (2024) 2521–2525.
- [40] S. Koziel, Computationally efficient multi-fidelity multi-grid design optimization of microwave structures, *App. Comp. EM Soc. J.* 25 (7) (2010) 578–586.
- [41] A. Conn, K. Scheinberg, L.N. Vicente, *Introduction to Derivative-Free Optimization*, MPS-SIAM Series on Optimization, Philadelphia, 2009.
- [42] A.V. Oppenheim, R.W. Schaffer, *Discrete-Time Signal Processing*, 3rd ed., Prentice Hall, 2009.
- [43] M.X. Cohen, *Analyzing Neural Time Series Data: Theory and Practice*, MIT Press, 2014.
- [44] T.K. Sarkar, O. Pereira, Using the matrix pencil method to estimate the parameters of a sum of complex exponentials, *IEEE Ant. Prop. Mag.* 37 (1) (1995) 48–55.
- [45] T.K. Sarkar, M. Salzar-Palma, M.D. Zhu, H. Chen, *Modern Characterization of Electromagnetic Systems and Its Associated Metrology*, Wiley IEEE Press, 2021.
- [46] J. Olencki, V. Waladi, A. Bekasiewicz, L. Leifsson, A low-cost system for far-field non-anechoic measurements of antenna performance figures, *IEEE Access* 11 (2023) 39165–39175.
- [47] M.V.T. Heckler, A. Dreher, Analysis of monopoles installed on airframes, *IEEE Ant. Prop. Soc. Inter. Symp.*, Washington DC, USA, 2005, pp. 280–283.
- [48] R. Buche, H.J. Kushner, Adaptive optimization of least-squares tracking algorithms: with applications to adaptive antenna arrays for randomly time-varying mobile communications systems, *IEEE Trans. Auto. Cont.* 50 (11) (2005) 1749–1760.
- [49] J.R. Mohammed, Comparative performance investigations of stochastic and genetic algorithms under fast dynamically changing environment in smart antennas, *Int. J. Elec. Comp. Eng.* 2 (1) (2012) 98–105.
- [50] T. Zou, A method to reduce correction error for electromagnetic wave propagation model, *Adva. Intel. Syst. Res.*, Atlantis Press, 2013, pp. 340–344.
- [51] I. Expósito, M.G. Sánchez, I. Cuiñas, Computing the influence of environmental conditions in electromagnetic measurements uncertainty, *IEEE Trans. Ant. Prop.* 67 (6) (2019) 4084–4090.
- [52] Y.-L. Song, et al., A magnetic field canceling system design for diminishing electromagnetic interference to avoid environmental hazard, *Int. J. Environ. Res. Public Health* 19 (6) (2022).
- [53] H.-H. Lee, et al., Estimation of electromagnetic field penetration into concrete buildings using a theoretical approach considering external environmental factors, *J. Electromagn. Eng. Sci.* 23 (3) (2023) 212–223.
- [54] S. Koziel, S. Ogurtsov, *Antenna design by simulation-driven optimization*, Springer, 2014.
- [55] S.F. Sawyer, Analysis of variance: the fundamental concepts, *J. Man. Manip. Ther.* 17 (2) (2009) 27–38.
- [56] Z. Wei, et al., Fast and automatic parametric model construction of antenna structures using CNN-LSTM networks, *IEEE Trans. Ant. Prop.*, 72 (2) (2024) 1319–1328.
- [57] M. Dzwonkowski, V. Waladi, A. Bekasiewicz, Multi-taper-based automatic correction of non-anechoic antenna measurements, *Metrologia* 61 (1) (2024) 1–9.